2019

Magnetic Field Monitoring in the SNS Neutron EDM Experiment

Alina Aleksandrova
University of Kentucky, aaal234@uky.edu
Digital Object Identifier: https://doi.org/10.13023/etd.2020.018

Recommended Citation

Aleksandrova, Alina, "Magnetic Field Monitoring in the SNS Neutron EDM Experiment" (2019). *Theses and Dissertations--Physics and Astronomy*. 68.
https://uknowledge.uky.edu/physastron_etds/68

STUDENT AGREEMENT:

I represent that my thesis or dissertation and abstract are my original work. Proper attribution has been given to all outside sources. I understand that I am solely responsible for obtaining any needed copyright permissions. I have obtained needed written permission statement(s) from the owner(s) of each third-party copyrighted matter to be included in my work, allowing electronic distribution (if such use is not permitted by the fair use doctrine) which will be submitted to UKnowledge as Additional File.

I hereby grant to The University of Kentucky and its agents the irrevocable, non-exclusive, and royalty-free license to archive and make accessible my work in whole or in part in all forms of media, now or hereafter known. I agree that the document mentioned above may be made available immediately for worldwide access unless an embargo applies.

I retain all other ownership rights to the copyright of my work. I also retain the right to use in future works (such as articles or books) all or part of my work. I understand that I am free to register the copyright to my work.

REVIEW, APPROVAL AND ACCEPTANCE

The document mentioned above has been reviewed and accepted by the student’s advisor, on behalf of the advisory committee, and by the Director of Graduate Studies (DGS), on behalf of the program; we verify that this is the final, approved version of the student’s thesis including all changes required by the advisory committee. The undersigned agree to abide by the statements above.

Alina Aleksandrova, Student

Dr. Bradley Plaster, Major Professor

Dr. Christopher Crawford, Director of Graduate Studies

MAGNETIC FIELD MONITORING IN THE SNS NEUTRON EDM EXPERIMENT

DISSERTATION

A dissertation submitted in partial
fulfillment of the requirements for
the degree of Doctor of Philosophy
in the College of Arts and Sciences
at the University of Kentucky

By
Alina Aleksandrova
Lexington, Kentucky

Director: Dr. Bradley Plaster, Professor of Physics
Lexington, Kentucky
2019

ABSTRACT OF DISSERTATION

MAGNETIC FIELD MONITORING IN THE SNS NEUTRON EDM EXPERIMENT

It is a well known fact that the visible universe is made almost entirely of baryonic matter. Yet, this is also one of the greatest puzzles that physicists are trying to solve: Where did all of this matter come from in the first place? The Standard Model (SM) of particle physics predicts a baryon asymmetry that is much smaller than what is observed in nature. In order to try and explain this discrepancy, Sakharov (1967) postulated three necessary conditions for baryogenesis in the early universe. One of these is the requirement that charge conjugation (C) and the product of C and parity (P) symmetries are violated. Because the SM fails to generate the observed baryon asymmetry, additional sources of CP violation are needed in order to help reconcile theory and observation. Thus, physicists have been looking for extensions to the SM in search of an answer. The presence of a neutron Electric Dipole Moment (nEDM) would signal a new source of CP violation. A non-vanishing nEDM would provide evidence for the breaking of both parity (P) and time-reversal symmetry (T). Because CPT symmetry is assumed to be conserved and has not been found to be broken, this would signal CP violation.

To look for an nEDM, stored ultracold neutrons are placed in parallel and anti-parallel magnetic and electric fields and the Larmor precession frequency is carefully measured. A difference in the precession frequency of the neutrons in the two states of the fields would signal the existence of an nEDM. The current upper limit of the nEDM was set by the RAL-Sussex-ILL collaboration and stands at $d_n < 3.0 \times 10^{-26}$ e cm (90% CL). Currently a new cryogenic apparatus is under construction at the Spallation Neutron Source (SNS) at the Oak Ridge National Laboratory (ORNL) which aims to reduce the current upper limit by two orders of magnitude.

A central problem to all neutron EDM experiments is the generation of a highly uniform and stable magnetic field. Because the suppression of systematic effects that arise from magnetic field nonuniformities and temporal drifts is vital to the success of these experiments, it is important to have the ability to precisely control and monitor the magnetic field gradients inside of the experimental volume. However, it is not always possible to measure the field gradients within the region of interest directly. To remedy this issue in the SNS nEDM experiment, a field monitoring system has been designed and tested that will allow for the reconstruction of the field gradients inside of the fiducial volume using noninvasive measurements of the field components at discrete locations external to this volume. This document will outline the theoretical framework of our method and present the results of experimental and simulated studies performed and the engineering design for such a field monitoring system.

KEYWORDS: neutrons, electric dipole moment, magnetic field

Author's signature: Alina Aleksandrova

Date: December 12, 2019

MAGNETIC FIELD MONITORING IN THE SNS NEUTRON EDM EXPERIMENT

By
Alina Aleksandrova

Director of Dissertation: Bradley Plaster

Director of Graduate Studies: Christopher Crawford

Date: December 12, 2019

Dedicated to my parents Tatyana and Alexander, my sister Anya, and my husband Ben.

ACKNOWLEDGMENTS

I would like to express my gratitude to my advisor Dr.Bradley Plaster without whose guidance I would not be the scientist that I am today. I would like to thank him for his guidance, support and encouragement throughout my graduate career.

Thank you to my thesis committee for your guidance and your insightful comments during the writing of this thesis : Dr.Christopher Crawford, Dr.Wolfgang Korsch and Dr.Peter Hislop.

Thank you to Ryan Dadisman and to Nima Nouri for the numerous projects that we have collaborated on and the insightful discussions that we've had that have been so instrumental to my work.

Thank you to Dr.Bradley Filippone, Dr.Christopher Swank, Dr.Simon Slutsky, Robert Carr and Charles Osthelder, my colleagues at the California Institute of Technology, for your support during the testing of the third scale prototype array.

Thank you to Danielle Schaper, Laura Kelton and Lakshya Malhotra for your support, encouragement and friendship. Graduate school would not have been the same without you.

Thank you to my colleagues and friends in my lab for your support.

Thank you to my family for their support and encouragement on this journey.

Most of all, thank you to my husband Ben for his unwavering support. You have been my rock through the most difficult and the most rewarding part of my life and I could not have done it without you.

This material is based upon work supported by the U.S. Department of Energy, Office of Science, Office of Nuclear Physics, under Award Number DE-SC0014622.

TABLE OF CONTENTS

LIST OF TABLES

LIST OF FIGURES

CHAPTER 1

INTRODUCTION

"I see trees of green, red roses too
I see them bloom for me and you
And I think to myself what a wonderful world"

—Louis Armstrong

The universe is full of mysteries just waiting to be answered. One of the great questions in physics is "Why is there so much more visible matter than anti-matter in the universe?" We know that our moon and the planets in our solar system are made of baryonic matter: after all, the Apollo 11 crew survived their stay on the moon! If there were antimatter galaxies, we would observe gamma rays from the annihilation processes at the matter-antimatter boundaries of the Universe.

One way to characterize the matter-antimatter asymmetry is through the quantity η:

$$\eta \equiv \frac{n_B}{n_\gamma} \tag{1.1}$$

where n_B is the difference between the number density of baryons and anti-baryons ($n_B = n_b - n_{\bar{b}}$) and n_γ is the number density of the photons. This ratio can be determined from the measurements done by WMAP[1] and Planck[2] of the temperature fluctuations in the cosmic microwave background (CMB)[3, 4, 5].

$$\eta \approx 6 \times 10^{-10}. \tag{1.2}$$

Another method is to look at the abundance of light elements such as deuterium, ^3He, ^4He and ^7Li [5, 6, 7] that were produced from Big Bang Nucleosynthesis (BBN). The abundance of these elements is highly dependent on η [8], thus, by determining[1] the primordial abundance of these elements one can get another value for η:

$$5.1 \times 10^{-10} < \eta < 6.7 \times 10^{-10}. \tag{1.3}$$

One can theoretically calculate the expected ratio η from the proton anti-proton annihilation cross section [10]. Assuming the universe started from a symmetric state ($\eta = 0$),

$$\eta = \frac{n_b}{n_\gamma} \simeq \frac{n_{\bar{b}}}{n_\gamma} \approx \left(\frac{m_p}{T}\right)^{3/2} e^{-m_p/T} \approx 10^{-18} \tag{1.4}$$

---

[1] The light nuclei abundances are not observed directly but are inferred from cosmological observations. For a detailed discussion refer to [9].

where m_p is the proton mass and $T \approx 20$ MeV[2]. It is clear that the theoretical result is much smaller than the asymmetry observed! Why is this the case?

While the Standard Model has been incredibly successful in describing all of the particles and interactions that are known from experiment, it has not been able to provide an answer to this intriguing question. Thus, physicists have begun to look for physics beyond the Standard Model in hopes of finding an answer. One such search is to find the electric dipole moment of the neutron (nEDM). A nEDM is an observable that can be measured and could help in the search for an answer!

This thesis, whose outline is described below, will focus on one such experiment that will take place at the Spallation Neutron Source (SNS) at the Oak Ridge National Laboratory (ORNL).

Chapter 2 will focus on the theoretical background where I will introduce and discuss the details of discrete symmetries P, C and T. The discovery of various symmetry violations will also be discussed along with how such violations led to the search for the nEDM. Chapter 3 will touch on some of the methods used in nEDM measurements and Chapter 4 will discuss the details of the nEDM experiment that will take place at the SNS. Chapter 5 will present a detailed analysis of systematic errors that arise from the nonuniformities in the magnetic field and how a magnetic field monitor will help to minimize such errors. A detailed discussion of the design and studies of such a field monitor will be presented. Concluding remarks will be made in Chapter 6.

---

[2] The temperature at which the annihilation rate, Γ_a, "freezes out" which happens when Γ_a is on the order of the expansion rate of the universe. [3, 10]

CHAPTER 2

THEORETICAL BACKGROUND

2.1 Fundamental Symmetries

One might wonder “What is symmetry?” and why is it so important? In physics, a symmetry is some transformation that leaves the Hamiltonian of the system unchanged.

In physics it is a well known fact that every continuous symmetry in nature yields a conservation law as was proven by Emmy Noether in 1917. For example, if a system is invariant under time translations, then energy is conserved. Similarly, the conservation of charge comes from the invariance of electrodynamics under gauge transformations [11].

In addition to continuous symmetries, there exist discrete symmetries and they describe non continuous changes to a system. For example, a square possesses discrete rotational symmetry as shown in Fig.2.1 while a circle possesses continuous symmetry.

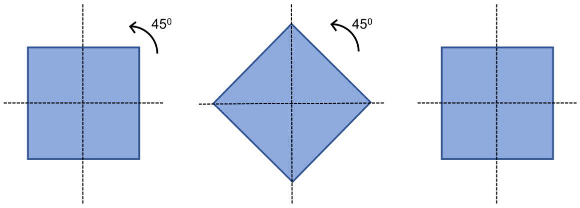

Figure 2.1: Discrete rotational symmetry

The discrete symmetries of interest are parity symmetry (P), charge conjugation (C) and time reversal symmetry (T). Each of these will be discussed in the following sections.

2.1.1 Parity Transformation

A parity transformation is defined by the inversion of the spatial coordinates.

$$\mathbf{P}^\dagger \vec{r}(x,y,z)\mathbf{P} = -\vec{r}(x,y,z). \tag{2.1}$$

A quantity that remains unchanged under a parity transformation is said to be invariant, or symmetric, with respect to this symmetry. For example, the angular momentum of a system is invariant under a parity transformation.

$$\begin{aligned} \mathbf{P}^\dagger \vec{L}\mathbf{P} &= \mathbf{P}^\dagger(\vec{r} \times m\vec{v})\mathbf{P} \\ &= -\vec{r} \times -m\vec{v} = \vec{r} \times m\vec{v} \\ &= \vec{L}. \end{aligned} \tag{2.2}$$

This also allows us to define polar and pseudo vectors, where a polar vector is a vector that changes sign under parity transformation, such as $\vec{r}$, and a pseudovector is invariant under this transformation, such as $\vec{L}$. Table 2.1 shows how various objects transform under parity.

Table 2.1: Transformation of Scalars and Vectors Under Parity

Object	Transformation under **P**
scalar	invariant: $\mathbf{P}^{\dagger}s\mathbf{P} \to s$
pseudoscalar	variant: $\mathbf{P}^{\dagger}p\mathbf{P} \to -p$
vector (polar vector)	variant: $\mathbf{P}^{\dagger}\vec{v}\mathbf{P} \to -\vec{v}$
pseudovector (axial vector)	invariant: $\mathbf{P}^{\dagger}\vec{a}\mathbf{P} \to \vec{a}$

Parity transformation changes the handedness of a system, i.e. a right-handed system becomes left-handed under this discrete transformation.

2.1.2 Charge Conjugation

Charge conjugation is an operation that transforms a particle into its corresponding antiparticle by changing the sign of the quantum numbers such as charge, baryon number, and lepton number.

For a charged particle in an electromagnetic field the Hamiltonian is given by Eq.2.3.

$$\mathbf{H} = \frac{1}{2m}(\vec{p} - q\vec{A}(\vec{r},t))^2 + q\phi(\vec{r},t) \tag{2.3}$$

where $\vec{A}(\vec{r},t)$ is the magnetic vector potential[1], q is the charge of the particle, and $V(\vec{r},t)$ is the electric scalar potential[2]. One can see how the Hamiltonian transforms under charge conjugation (C) by observing how each quantity transforms under C.

Table 2.2: Transformation of Objects Under Charge Conjugation

Physical Quantities	Transformation under **C**
$\vec{p}$	invariant: $\mathbf{C}^{\dagger}\vec{p}\mathbf{C} \to \vec{p}$
$\vec{A}$	variant: $\mathbf{C}^{\dagger}\vec{A}\mathbf{C} \to -\vec{A}$
ϕ	variant: $\mathbf{C}^{\dagger}\phi\mathbf{C} \to -\phi$
q	variant: $\mathbf{C}^{\dagger}q\mathbf{C} \to -q$

It is evident from Table 2.2 that the Hamiltonian is invariant under C transformation.

---

[1] $\vec{A}(\vec{r},t) = \frac{\mu_0}{4\pi}\int_{\Omega}\frac{\vec{J}(\vec{r}',t)}{|\vec{r}-\vec{r}'|}d^3\vec{r}'$

[2] $\phi(\vec{r},t) = \frac{1}{4\pi\epsilon_0}\int_{\Omega}\frac{\rho(\vec{r}',t)}{|\vec{r}-\vec{r}'|}d^3\vec{r}'$

2.1.3 Time Reversal Transformation

Cher once sang "If I could turn back time...", well, a time reversal transformation would do just that, in other words, $\mathbf{T}^\dagger \psi(t, \vec{r})\mathbf{T} \rightarrow \psi(-t, \vec{r})$. The time reversal operator, $\mathbf{T}$, will act on any time component while leaving any position object invariant. Table 2.3 shows how various quantities transform under time reversal.

Table 2.3: Transformation of Objects Under Time Reversal

Physical Quantities	Transformation under $\mathbf{T}$
$\vec{r}$	invariant: $\mathbf{T}^\dagger \vec{r}\mathbf{T} \rightarrow \vec{r}$
$\vec{p}$	variant: $\mathbf{T}^\dagger \vec{p}\mathbf{T} \rightarrow -\vec{p}$
$\vec{L}$	variant: $\mathbf{T}^\dagger \vec{L}\mathbf{T} \rightarrow -\vec{L}$

An important property of the time reversal operator, $\mathbf{T}$, is that it must be antiunitary[3]. Why must this be so? We know that the commutation relation $[\hat{x}, \hat{p}] = -\imath\hbar$[4] must always hold. But, unless $\mathbf{T}^\dagger \imath \mathbf{T} = -\imath$, then we will not preserve the canonical commutator. We can also prove this by considering the time evolution of a state $|\psi(\vec{r}, t)\rangle = \mathbf{U}\,|\psi(\vec{r}, 0)\rangle$, where $\mathbf{U} = e^{\frac{-\imath \mathbf{H} t}{\hbar}}$ is the time evolution operator, and applying time reversal to it.

$$\mathbf{T}\,|\psi(\vec{r}, t)\rangle = \mathbf{T}e^{-\frac{\imath \mathbf{H} t}{\hbar}}\,|\psi(\vec{r}, 0)\rangle \tag{2.4}$$

If the motion of the system is invariant under $\mathbf{T}$ reversal, then Eq.2.4 should be equivalent to first applying $\mathbf{T}$ at some $t = 0$ and then letting the system evolve to an earlier moment $t \rightarrow -t$.

$$e^{-\frac{\imath \mathbf{H}(-t)}{\hbar}}\mathbf{T}\,|\psi(\vec{r}, 0)\rangle \tag{2.5}$$

thus

$$\mathbf{T}e^{-\frac{\imath \mathbf{H} t}{\hbar}}\,|\psi(\vec{r}, 0)\rangle = e^{\frac{\imath \mathbf{H} t}{\hbar}}\mathbf{T}\,|\psi(\vec{r}, 0)\rangle \tag{2.6}$$

.

Now, for small t, the time evolution operator in Eq.2.6 can be expanded as follows:

$$\mathbf{T}(1 - \frac{\imath \mathbf{H} t}{\hbar})\,|\psi(\vec{r}, 0)\rangle = (1 + \frac{\imath \mathbf{H} t}{\hbar})\mathbf{T}\,|\psi(\vec{r}, o)\rangle \tag{2.7}$$

and

$$-\mathbf{T}\imath\mathbf{H}\,|\psi(\vec{r}, 0)\rangle = \imath\mathbf{H}\mathbf{T}\,|\psi(\vec{r}, 0)\rangle\,. \tag{2.8}$$

---

[3] An antiunitary operator satisfies $\mathbf{T}\mathbf{T}^\dagger = -I$ while a unitary operator satisfies $\mathbf{O}\mathbf{O}^\dagger = I$.

[4] $[\hat{x}, \hat{p}] = \hat{x}\hat{p} - \hat{p}\hat{x} = -\imath\hbar$

Eq.2.8 implies that

$$-\mathbf{T}\imath\mathbf{H} = \imath\mathbf{H}\mathbf{T} \tag{2.9}$$

and if $\mathbf{T}$ is a unitary[5] operator, then

$$-\mathbf{T}\mathbf{H} = \mathbf{H}\mathbf{T} \tag{2.10}$$

which implies that $\mathbf{T}$ and $\mathbf{H}$ anticommute[6]:

$$\{\mathbf{H}, \mathbf{T}\} = 0 \tag{2.11}$$

However, this leads us to a problem! We know that

$$\mathbf{H} |\psi_n\rangle = E_n |\psi_n\rangle \tag{2.12}$$

where $|\psi_n\rangle$ is an eigenstate corresponding to the eigenvalue E_n. From the anticommutation relation of Eq.2.11, it follows that

$$\mathbf{H}\mathbf{T} |\psi_n\rangle = -\mathbf{T}\mathbf{H} |\psi_n\rangle = -E_n\mathbf{T} |\psi_n\rangle \tag{2.13}$$

where $\mathbf{T} |\psi_n\rangle$ is an eigenstate which corresponds to eigenvalue $-E_n$. This means that given some eigenstate of $\mathbf{H}$, the time reversed state would have negative energy. However, this does not make physical sense as it leads to an energy spectrum which is not bounded from below! Thus, to correct for this, $\mathbf{T}$ must be antiunitary:

$$\mathbf{T}\imath\mathbf{T}^\dagger = -\imath \tag{2.14}$$

In this case, $\mathbf{H}$ and $\mathbf{T}$ commute[7], $[\mathbf{H}, \mathbf{T}] = 0$, and Eq.2.13 becomes

$$\mathbf{H}\mathbf{T} |\psi_n\rangle = \mathbf{T}\mathbf{H} |\psi_n\rangle = E_n\mathbf{T} |\psi_n\rangle . \tag{2.15}$$

2.2 Symmetry Violation

2.2.1 C, P, T Violation

It has been a firm held belief that nature ought to be symmetric with respect to parity transformation, charge conjugation, and time reversal; it was preposterous to even suggest that there could be violation of these fundamental symmetries. It was not until 1956, when Lee and Yang [12] questioned the assumption that parity invariance is self-evident. While there was no evidence that parity was broken in the strong and electromagnetic interactions, no one had ever tested for parity invariance in the weak interaction. And so the belief of parity invariance came crashing down with the discovery of parity violation in the β decay of ^{60}Co in an experiment carried out by

---

[5] A unitary operator satisfies $\mathbf{U}\mathbf{U}^\dagger = 1$.

[6] $\{\mathbf{H}, \mathbf{T}\} = \mathbf{H}\mathbf{T} + \mathbf{T}\mathbf{H} = 0$

[7] $[\mathbf{H}, \mathbf{T}] = \mathbf{H}\mathbf{T} - \mathbf{T}\mathbf{H} = 0$

C.S. Wu et al. [13]. Thus parity violation became an essential part of weak interaction theory.

Weak interactions are also not invariant under C as can be illustrated via μ^- decays.

$$\mu^- \rightarrow e^- + \nu_\mu + \overline{\nu}_e \tag{2.16}$$

It is known that neutrinos are always left-handed and antineutrinos are always right-handed. Applying C on Eq.2.16 results in

$$\mu^+ \rightarrow e^+ + \overline{\nu}_\mu + \nu_e \tag{2.17}$$

In the case of Eq.2.17, the left-handed neutrino is transformed into a left-handed antineutrino, which is not physical! Thus C is not a good symmetry!

The only comfort found was that the combined charge conjugation and parity (CP) operations are invariant. For the reaction above, C would produce a left-handed antineutrino and P would turn the left-handed antineutrino into a right handed one, producing a physical result! Yet this state of comfort did not last long as CP symmetry was also found to be violated by Cronin and Fitch in their experiment with K^0 decays in 1963 [14].

And so, like dominoes, the long held belief of the invariance of these symmetries came crashing down. For, if P and C are not invariant in the weak interaction, why shouldn't T be violated as well? It is generally accepted that CPT is a fundamental symmetry of nature and there has yet to be experimental evidence that it is broken. Thus CP violation indicates that T violation must also be found in nature[8].

2.2.2 CP Violation and the Sakharov Conditions

So how does symmetry violation lead one to the search for the neutron electric dipole moment?

In 1967, Andrei Sakharov proposed three necessary conditions [10, 16], which must be simultaneously satisfied, in order to explain how the universe evolved into a baryon asymmetric state:

1. **Baryon number violation must be present in some process.**

    The violation of baryon number is a minimum starting point that would lead us to the baryon asymmetry of the universe. If the universe started as a baryon-symmetric state and if every fundamental interaction conserves baryon number (B-number) individually, then B-number should be conserved globally. If this is the case, there should be no observed baryon asymmetry. Thus, there must be some process that produces extra baryons.

---

[8] The BaBar experiment has directly measured T violation [15].

2. **C and CP violation must be present in nature.**

   However, B-number violation by itself is not enough – there needs to be C and CP violation present. Why is this the case? Suppose that there exists a B-violating process:

   $$A \to C + B \tag{2.18}$$

   where A and C have a baryon number of zero. This process produces an excess baryon. If C is always conserved then there will exist a corresponding C-conjugate reaction:

   $$\overline{A} \to \overline{C} + \overline{B} \tag{2.19}$$

   The rates (Γ) of the processes 2.18 and 2.19 would be the same and so, after some period of time, B-number would be conserved.

   $$\Gamma(A \to B + C) = \Gamma(\overline{A} \to \overline{C} + \overline{B}) \tag{2.20}$$

   It is clear that the rate of baryon production needs to be greater than that of the production of anti-baryons, which implies there must be C violation. Yet, on its own, C violation is not enough to tip the balance, CP violation must also be present.

   Suppose there exists some decay process where some particle D decays into either two left handed or two right handed quarks:

   $$\begin{aligned} D &\to q_R q_R \\ D &\to q_L q_L \end{aligned} \tag{2.21}$$

   C violation implies that:

   $$\Gamma(D \to q_L q_L) \neq \Gamma(\overline{D} \to \overline{q}_R \overline{q}_R) \tag{2.22}$$

   On the other hand, CP conservation implies that:

   $$\begin{aligned} \Gamma(D \to q_R q_R) &= \Gamma(\overline{D} \to \overline{q}_L \overline{q}_L) \\ \Gamma(D \to q_L q_L) &= \Gamma(\overline{D} \to \overline{q}_R \overline{q}_R) \end{aligned} \tag{2.23}$$

   Thus, even though C is not conserved which creates some baryon asymmetry, summing over all of the helicities would restore the balance between baryon and antibaryon production:

   $$\Gamma(D \to q_L q_L) + \Gamma(D \to q_R q_R) = \Gamma(\overline{D} \to \overline{q}_R \overline{q}_R) + \Gamma(\overline{D} \to \overline{q}_L \overline{q}_L) \tag{2.24}$$

   So both C and CP violation must be present in nature to have a baryon asymmetric universe.

3. **Departure from thermodynamic equilibrium.**

In order for baryon number (B) asymmetry to be present in the universe, any process that generates B abundance must occur outside of thermal equilibrium. In order to show the necessity of this condition, one can calculate the average value of B in thermodynamic equilibrium.

The equilibrium average of the baryon number operator at some temperature, T can be expressed as follows [17]:

$$\begin{aligned}\langle B(t)\rangle_T &= Tr\Big(e^{-\frac{H}{T}}B(t)\Big)\\ &= Tr\Big(e^{-\frac{H}{T}}e^{-iHt}B(0)e^{iHt}\Big)\\ &= Tr\Big(e^{iHt}e^{-\frac{H}{T}}e^{-iHt}B(0)\Big)\\ &= \langle B(0)\rangle_T\end{aligned} \tag{2.25}$$

We can also show that $\langle B(0)\rangle_T = -\langle B(0)\rangle_T$ as follows[9]:

$$\begin{aligned}\langle B(0)\rangle_T &= Tr\Big[\Theta\Theta^\dagger e^{-\frac{H}{T}}B(0)\Big]\\ &= Tr\Big[\Theta^\dagger e^{-\frac{H}{T}}B(0)\Theta\Big]\\ &= -\langle B(0)\rangle_T\end{aligned} \tag{2.26}$$

To verify the validity of Eq. 2.26, one must first express the baryon number in terms of the quark fields, $q(\vec{x},t)$ and show how it transforms under C, P and T transformations [10]:

$$\widehat{B} = \frac{1}{3}\sum_q \int d^3x : q^\dagger(\mathbf{x},t)q(\mathbf{x},t) :\ ^{10} \tag{2.27}$$

How does Eq. 2.27 transform under the P transformation?

$$P\widehat{B}P^{-1} = P : q^\dagger(\mathbf{x},t)q(\mathbf{x},t) : P^{-1} \tag{2.28}$$

From 2.1.1, one can see that the quark fields will transform as [18]:

$$\begin{aligned}Pq(\mathbf{x},t)P^{-1} &= \gamma^0 q(\mathbf{x},t)\\ Pq^\dagger(\vec{x},t)P^{-1} &= q^\dagger(-\mathbf{x},t)\gamma^0\end{aligned} \tag{2.29}$$

under P. Here γ^0 denotes the Dirac matrix[11]. Thus,

$$\begin{aligned}P\widehat{B}P^{-1} &= P : q^\dagger(\mathbf{x},t)q(\mathbf{x},t) : P^{-1}\\ &=: q^\dagger(-\mathbf{x},t)q(-\mathbf{x},t) :\\ &= \widehat{B}\end{aligned} \tag{2.30}$$

---

[9] Here $\Theta = CPT$ and $\Theta^\dagger = C^(-1)P^(-1)T^(-1)$.

[10] The Baryon number operator is given by $\int d^3x J_0^B(x)$ where J_0^B is the associated Noether current: $\sum\limits_q \frac{1}{3}\overline{q}\gamma_0 q$ and $\overline{q} = q^\dagger\gamma^0$ [11, 18]

[11] $\begin{pmatrix} I_2 & 0 \\ 0 & -I_2 \end{pmatrix}$ where I_2 is the identity matrix

How does Eq. 2.27 transform under the C conjucation transformation?

$$C\widehat{B}C^{-1} = C : q^{\dagger}(\mathbf{x},t)q(\mathbf{x},t) : C^{-1} \tag{2.31}$$

From 2.1.2, one can see that the quark fields will transform as [18]:

$$\begin{aligned} Cq(\mathbf{x},t)C^{-1} &= i\gamma^2 q^{\dagger}(\mathbf{x},t) \\ Cq^{\dagger}(\mathbf{x},t)C^{-1} &= iq^{\dagger}(\mathbf{x},t)\gamma^2 \end{aligned} \tag{2.32}$$

under C, where γ^2 is the Dirac matrix[12]. Thus,

$$\begin{aligned} C\widehat{B}C^{-1} &= C : q^{\dagger}(\mathbf{x},t)q(\mathbf{x},t) : C^{-1} \\ &= - : q^{\dagger}(\mathbf{x},t)q(\mathbf{x},t) : \\ &= -\widehat{B} \end{aligned} \tag{2.33}$$

How does Eq. 2.27 transform under the T reversal transformation?

$$T\widehat{B}T^{-1} = T : q^{\dagger}(\mathbf{x},t)q(\mathbf{x},t) : T^{-1} \tag{2.34}$$

From 2.1.3, one can see that the quark fields will transform as [18]:

$$\begin{aligned} Tq^{\dagger}(\mathbf{x},t)T^{-1} &= -iq^{\dagger}(\mathbf{x},t)\gamma_5\gamma^0\gamma^2 \\ Tq(\mathbf{x},t)T^{-1} &= -i\gamma_5\gamma^0\gamma^2 q^{\dagger}(\mathbf{x},t) \end{aligned} \tag{2.35}$$

under T, where $\gamma_5 = i\gamma^0\gamma^1\gamma^2\gamma^3$ and is a Dirac matrix[13]. Thus,

$$\begin{aligned} T\widehat{B}T^{-1} &= T : q^{\dagger}(\mathbf{x},t)q(\mathbf{x},t) : T^{-1} \\ &=: q^{\dagger}(\mathbf{x},-t)q(\mathbf{x},-t) : \\ &= \widehat{B}. \end{aligned} \tag{2.36}$$

Finally, one can show that under the combined CPT transformation:

$$\begin{aligned} \Theta\widehat{B}\Theta^{-1} &= \Theta : q^{\dagger}(\mathbf{x},t)q(\mathbf{x},t) : \Theta^{-1} \\ &= - : q^{\dagger}(-\mathbf{x},-t)q(-\mathbf{x},-t) : \\ &= -\widehat{B}. \end{aligned} \tag{2.37}$$

It is clear that in order to have an excess number of baryons, any process that generates a baryon number asymmetry must occur outside of thermodynamic equilibrium.

---

[12] $\begin{pmatrix} 0 & \sigma_2 \\ -\sigma_2 & 0 \end{pmatrix}$ where σ_2 is the Pauli spin matrix $\begin{pmatrix} 0 & -i \\ i & 0 \end{pmatrix}$

[13] $\begin{pmatrix} 0 & I_2 \\ I_2 & 0 \end{pmatrix}$ where I_2 is the identity matrix.

While baryon number violation has yet to be observed experimentally, the Standard Model (SM) of particle physics does account the CP violation observed in the K, B, and D meson systems.

It appears as an imaginary phase in the Cabibbo-Kobayashi-Maskawa (CKM) [19] mixing matrix, V.

$$V = \begin{pmatrix} V_{ud} & V_{us} & V_{ub} \\ V_{cd} & V_{cs} & V_{cb} \\ V_{td} & V_{ts} & V_{tb} \end{pmatrix} \tag{2.38}$$

The CKM matrix relates the weak eigenstates (d', s', b') to the mass eigenstates (d, s, b) in the quark sector. In hadronic weak interactions, it is the quark mass eigenstates that form the observable quantities.

$$\begin{pmatrix} d' \\ s' \\ b' \end{pmatrix} = \begin{pmatrix} V_{ud} & V_{us} & V_{ub} \\ V_{cd} & V_{cs} & V_{cb} \\ V_{td} & V_{ts} & V_{tb} \end{pmatrix} \begin{pmatrix} d \\ s \\ b \end{pmatrix} \tag{2.39}$$

Quark masses are generated by coupling to the Higgs field and the matrix elements correspond to the coupling constants of the up-type[14] and down-type quarks. Because there are three families of quarks, the CKM matrix can be parametrized by four independent parameters: three real mixing angles θ_{12}, θ_{13} and θ_{23} as well as an irreducible imaginary phase δ [20].

$$\begin{pmatrix} d' \\ s' \\ b' \end{pmatrix} = \begin{pmatrix} c_{12}c_{13} & s_{12}c_{13} & s_{13}e^{-i\delta} \\ -s_{12}c_{23} - c_{12}s_{23}s_{13}e^{i\delta} & c_{12}c_{23} - s_{12}s_{23}s_{13}e^{i\delta} & s_{23}c_{13} \\ s_{12}s_{23} - c_{12}c_{23}s_{13}e^{i\delta} & -c_{12}s_{23} - s_{12}c_{23}s_{13}e^{i\delta} & c_{23}s_{13} \end{pmatrix} \begin{pmatrix} d \\ s \\ b \end{pmatrix} \tag{2.40}$$

where c_i and s_i represent $\cos\theta_i$ and $\sin\theta_i$ respectively (here $i = 1, 2, 3$). The CKM mixing matrix enters in the charged-current weak interaction Langrangian [21]:

$$\mathcal{L}_W^q = \frac{g_W}{\sqrt{2}}(W_\mu^+ \overline{u}_L \gamma^\mu V d_L + W_\mu^- \overline{d}_L \gamma^\mu V^\dagger u_L). \tag{2.41}$$

If the phase $\delta \neq 0, \pi$, Eq. 2.41 is not invariant under CP[15].

CP violation can also be found in the strong interaction and arises from the $\overline{\theta}$ term [22].

$$\mathcal{L}_{QCD}^{eff} = \mathcal{L}_{QCD} + \frac{g_s^2}{32\pi^2}\overline{\theta} G_{\mu\nu}^a \widetilde{G}^{\mu\nu,a} \tag{2.42}$$

where $G^{\mu\nu}$ is the gluon field, $\widetilde{G}_{\mu\nu}$ is its dual and $\overline{\theta} \equiv \theta + Arg[Det(M_q)]$ [23]. The most stringent constraint on the $\overline{\theta}$ terms comes from the neutron electric dipole moment

---

[14] Up-type quarks correspond to quarks that have charge $+\frac{2}{3}e$ such as the up, charm and top quarks. Down-type quarks correspond to those of charge $-\frac{1}{3}e$ such as down, strange and bottom.

[15] This is explicitly shown in [21] pg. 162–163.

$d_n \approx (10^{-16}\overline{\theta})$e cm [21, 24]. With the current experimental limit for $d_n < 3.0 \times 10^{-26}$ [25], this bounds $|\overline{\theta}| < 10^{-10}$. However, as the QCD vacuum angle, it is expected to be of order unity [26]. Why is this term so small? This is known as the strong CP problem and is an outstanding question in physics. A possible solution to this problem was proposed by Peccei and Quinn [27, 28, 29]. The Peccei-Quinn mechanism introduces a new global symmetry, $U(1)_{PQ}$, that is spontaneously broken and results in the Nambu-Goldstone boson called the axion.

$$\overline{\theta} \rightarrow \frac{a(x)}{f_{PQ}} \tag{2.43}$$

where $a(x)$ is the axion field and f_{PQ} is the Peccei-Quinn order parameter associated with the symmetry breaking. This causes the $\overline{\theta}$ term to become a dynamical field whose potential minimizes at $\overline{\theta} = 0$ [30, 31, 32].

While the SM accounts for the CP violation observed in the K, B, and D meson systems, it cannot account for the observed matter-antimatter asymmetry and physicists are searching for new CP-violating interactions.

2.2.3 The Standard Model and the Neutron Electric Dipole Moment

An interesting consequence of CP violation is that elementary particles, one of which being the neutron, would have an electric dipole moment. Thus, if one can measure an electric dipole moment of the neutron (nEDM), one could point to another source of CP violation in the Standard Model, thus helping lead to the resolution of the matter-antimatter asymmetry.

An electric dipole moment (EDM) for a pair of opposite charges (q and -q) is defined to be

$$\vec{d} = q\vec{r} \tag{2.44}$$

where $\vec{r}$ is the distance between the charges q and $-q$ and the defined direction for the dipole moment is from the negative to positive charge as illustrated in Fig.2.2.

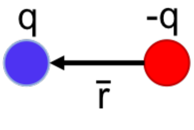

Figure 2.2: Diagram of an electric dipole moment.

For a system comprised of many charged constituents, Eq.2.44 can be redefined as:

$$\vec{d} = \sum_i q_i \vec{r}_i \tag{2.45}$$

While the neutron is electrically neutral, if there is any displacement between the charged internal constituents[16] and the center of mass, it can have an electric dipole moment (EDM). Such an EDM would violate both parity and time reversal symmetries. This can be understood by examining the interaction Hamiltonian of a neutron in the presence of electric and magnetic fields.

Suppose a neutron with spin $\vec{s}$ moves through some electric and magnetic fields, $\vec{E}$ and $\vec{B}$. If the neutron has an electric dipole moment d_n it will interact with these fields via:

$$H = -(\mu_n \vec{B} + d_n \vec{E}) \cdot \frac{\vec{s}}{|\vec{s}|} \tag{2.46}$$

where γ_n is the gyromagnetic ratio of the neutron and $\vec{s}$ is the neutron spin. Table 2.4 shows that the interaction Hamiltonian is odd under both P and T transformations. The T violation arises from the $\vec{s} \cdot \vec{E}$ term associated with the EDM. This T violation implies CP violation via the CPT theorem.

Table 2.4: P and T violation of electric dipole moment

Physical Quantities	**P**	**T**
Spin: $\vec{s}$	$+$	$-$
Electric field: $\vec{E}$	$-$	$+$
Magnetic field: $\vec{B}$	$+$	$-$

Thus, in order to generate an nEDM, there must be CP violation. The SM prediction for the nEDM lies in the $d_n \approx 10^{-32} - 10^{-34}$ e cm range [33, 34, 35].

It can be concluded that new physics is needed to help explain the BAU in the universe, and the neutron EDM could lead the way to reconciling theory and observation.

---

[16] A neutron is comprised of one *u*-quark and two *d*-quarks.

CHAPTER 3

MEASURING A NEUTRON ELECTRIC DIPOLE MOMENT

3.1 Measuring a Neutron Electric Dipole Moment

How does one measure a neutron EDM, d_n? The primary method used to determine d_n is to examine the precession frequency of the neutron spin under various conditions of electric and magnetic fields.

Recall the Hamiltonian given in Eq. 2.46: $\mathrm{H} = -(\mu_n \vec{B} + d_n \vec{E}) \cdot (\vec{s}/|\vec{s}|)$. When the neutron interacts with the magnetic and electric fields, the neutron spin will experience a torque causing a change in the angular momentum of the system. This results in the precession of the neutron spin about the $\vec{E}$ and $\vec{B}$ fields. If the $\vec{E}$ and $\vec{B}$ fields are aligned with each other, the frequency at which the neutron precesses is given by

$$\omega_{\uparrow\uparrow} = \left|\gamma_n B + \frac{2d_n E}{\hbar}\right| \tag{3.1}$$

where $\uparrow\uparrow$ indicates that $\vec{E}$ and $\vec{B}$ are parallel to each other. For the case of $\vec{E}$ and $\vec{B}$ anti-parallel, the precession frequency is given by

$$\omega_{\uparrow\downarrow} = \left|\gamma_n B - \frac{2d_n E}{\hbar}\right|. \tag{3.2}$$

Thus, by reversing the direction of $\vec{E}$ with respect to $\vec{B}$ and measuring the difference in the precession frequency of the neutron spin, the electric dipole moment can be determined via Eq. 3.3.

$$d_n = \frac{\hbar \Delta\omega}{4|\vec{E}|} \tag{3.3}$$

where $\Delta\omega = \omega_{\uparrow\uparrow} - \omega_{\uparrow\downarrow}$.

Historically, the most sensitive searches for the nEDM aim to measure such a difference in the precession frequency. The figure of merit used to compare different nEDM experiment can be derived from the energy equation:

$$\varepsilon = \hbar\omega = \vec{d} \cdot \vec{E} \tag{3.4}$$

which leads to the uncertainty[1]:

$$\sigma_d \sim \frac{\hbar}{|\vec{E}|T} \tag{3.5}$$

---

[1] Here we have used the Uncertainty Principle, $\Delta\varepsilon\Delta t \sim \hbar$, which states that in order to get a precise energy measurement, a long measurement time is needed.

where $|\vec{E}|$ is the strength of the applied electric field and T is the length of the neutron precession measurement. The precision of the experiment can be increased by increasing the number of times the the frequency measurements are made. Thus, for an ensemble of N neutrons and a number of measurements m, the statistical uncertainty is given by [36]:

$$\sigma_d \sim \frac{1}{|\vec{E}|T\sqrt{mN}}. \tag{3.6}$$

From Eq. 3.6 it is evident that in order to minimize the statistical uncertainty, the experiment must have a large $\vec{E}$ field, a long measurement time and a large number of neutrons.

3.2 Historical Searches for the nEDM

The first measurement of the neutron electric dipole moment was made in 1951 by Smith, Ramsey and Purcell that set the limit of $-(0.1 \pm 2.4) \times 10^{-20}$e cm in 1957 [37]. This experiment was done using a neutron beam magnetic resonance method. Such beam experiments were used to push the sensitivity limit down by four orders of magnitude [38] until the systematic effects due to the high neutron velocities became too hard to overcome. The largest systematic effect for beam experiments [39] came from the motional magnetic field, or the magnetic field, $\vec{B}_m$, that is generated in the frame of the neutron due to its motion through a static electric field $\vec{E}$.

$$\vec{B}_m = \frac{\vec{E} \times \vec{v}}{c^2}. \tag{3.7}$$

This effect would result in the modification of the effective magnetic field in the experiment $\vec{B}_{eff} = \vec{B}_0 + \vec{B}_m$. Improvements in technology and experimental methods were needed in order to push the sensitivity limit even lower.

The present limit on neutron EDM experimnet was established by the experiment at the Institute Laue-Langevin (ILL) and stands at 3.0×10^{-26}e cm (90% CL) [25, 40]. Unlike the beam experiments that preceded it, the present limits on the nEDM are set by experiments which use ultracold neutrons (UCN).

Ultracold neutrons are neutrons whose energies are on the order of 300 neV ($v \approx 7$ m/s). One of the most special properties of UCNs is that, unlike more energetic neutrons, they can be totally internally reflected from surfaces of certain materials at any angle of incidence [41, 42]. This allows them to be stored in material bottles. Because ultracold neutrons can be stored, experiments that use them can achieve higher sensitivity measurements due to the increase of the interaction time. Figure 3.1 shows the improvement of the limit on the neutron EDM as a function of time.

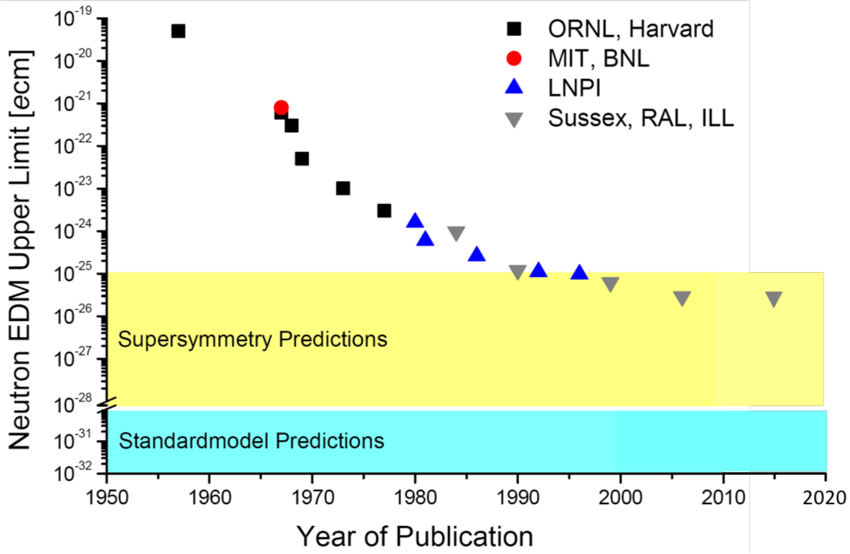

Figure 3.1: Measured upper limits of the neutron EDM. This plot was taken from Andreas Knecht and modified for this thesis to include the results from [25].

3.3 Neutron Precession Measurements

3.3.1 Ramsey Method of Separated Oscillatory Fields

A key method to measuring spin precession is Ramsey's method of separated oscillatory fields [43]. This method modifies the Rabi method (the derivation for which is shown in A) which relies on the probability of a spin flipping from its initial state upon the application of an oscillating magnetic field transverse to the direction of the polarization. The Ramsey method utilizes the Rabi spin flip but breaks it up into two $\pi/2$ pulses that are separated by a free precession time.

Fig.3.2 shows a diagram of the separated oscillatory field method. The right hand side shows the signal generating the perturbing field, B_{rf}. This will act as a reference clock for the Ramsey measurement as it will maintain a coherent phase throughout the duration of the measurement. The neutrons start polarized along the direction of the main holding field $B_{0\uparrow}$ with the perturbing field gated off. The B_{rf} field is then turned on and a $\frac{\pi}{2}$ pulse is applied for some time t, which tips the neutron spin into the plane perpendicular to $B_{0\uparrow}$. The perturbing field is then gated off and the neutron spins are allowed to precess freely for some time $T \gg t$ after which a second $\frac{\pi}{2}$ pulse is applied (coherent with the first). If the frequency of B_{rf} is in phase with the spin precession, the pulse will flip the spins by π with respect to the intitial polarization. If a phase difference between the perturbing field and the neutron precession frequency accumulates during the free precession time T, then the second $\frac{\pi}{2}$ pulse will be less efficient at flipping the spins.

Fig.3.3 shows a Ramsey fringe pattern where the number of neutrons remaining with their spins not flipped after a Ramsey measurement as a function of the perturbing

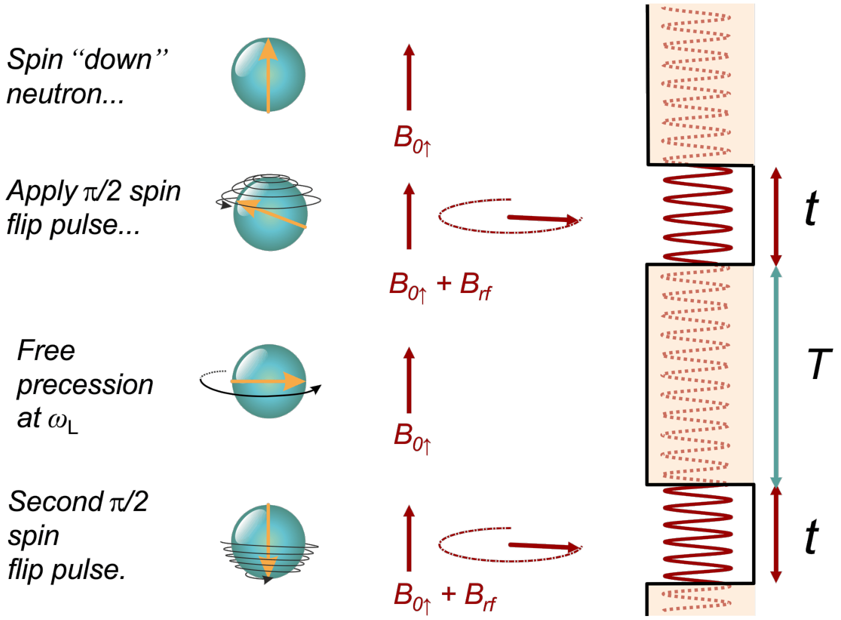

Figure 3.2: Ramsey's method of separated oscillatory fields schematic diagram. [44]

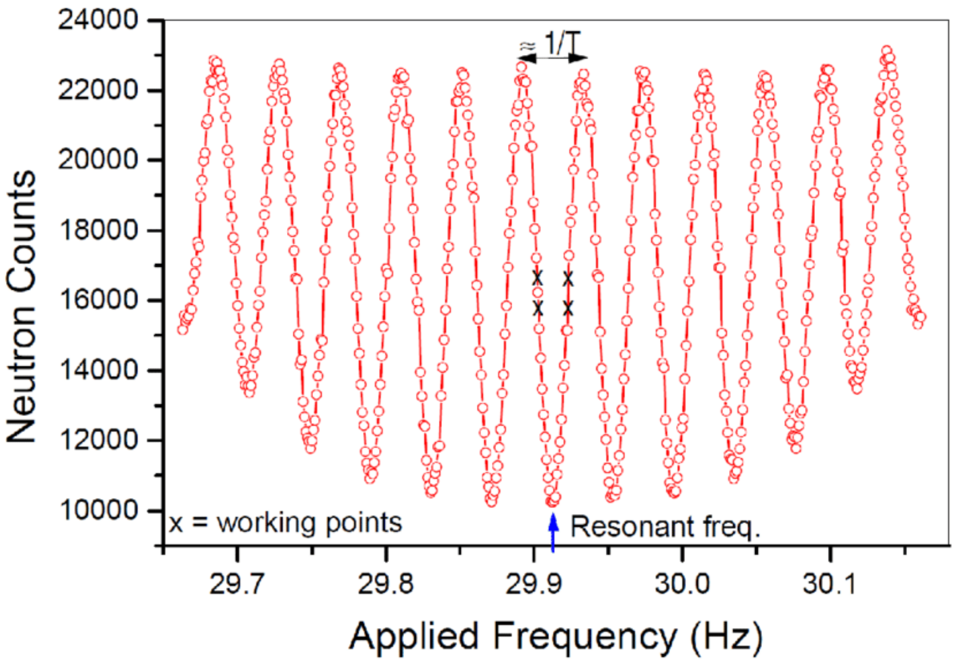

Figure 3.3: Ramsey fringe pattern.[44]

field frequency.

One experiment that utilizes the Ramsey method of separated oscillatory fields is the neutron EDM experiment at the Los Alamos National Laboratory (LANL) [35]. In this experiment the UCN are transported from the source into the measurement cell where the Ramsey method is used. The UCN are then unloaded into the spin

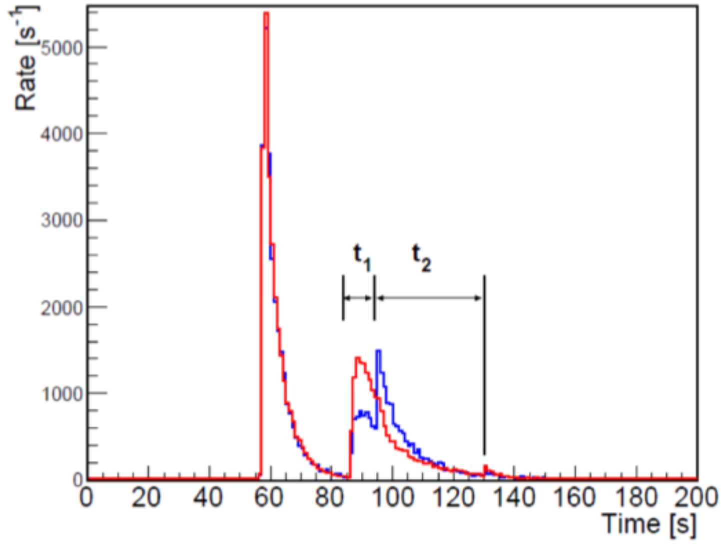

Figure 3.4: Neutron count rate for a 30 second holding time. Here t_1 represents the time to count neutrons of one spin state (peak at $\sim$ 85 seconds). The peak at t_2 represents the time to count neutrons of the other spin state after the analyzer spin flipper is turned on.

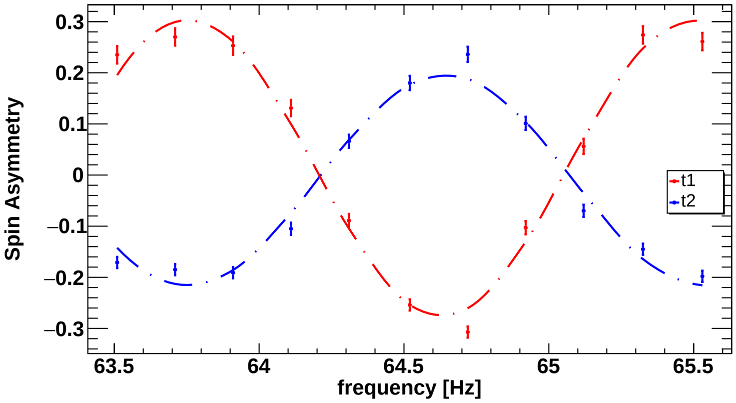

Figure 3.5: Measurement of the Rabi fringe pattern for a 1 second free precession time. Here the red line represents the spin asymmetry after counting time t_1 and the blue line represents the spin asymmetry after counting time t_2.

analyzer. Only one spin state can be counted at a time, so that in order to count both spin states, the analyzing procedure is split into two count times, t_1 and t_2 where one spin state is counted first followed by an analyzer spin flipper application in order to count the other spin state Fig.3.4. The Rabi and Ramsey fringes were measured during the experimental run in September 2017 and are shown in Figs.3.5 and 3.6. The data shown in these figures were collected and analyzed by A. Aleksandrova and Dr. J. Long.

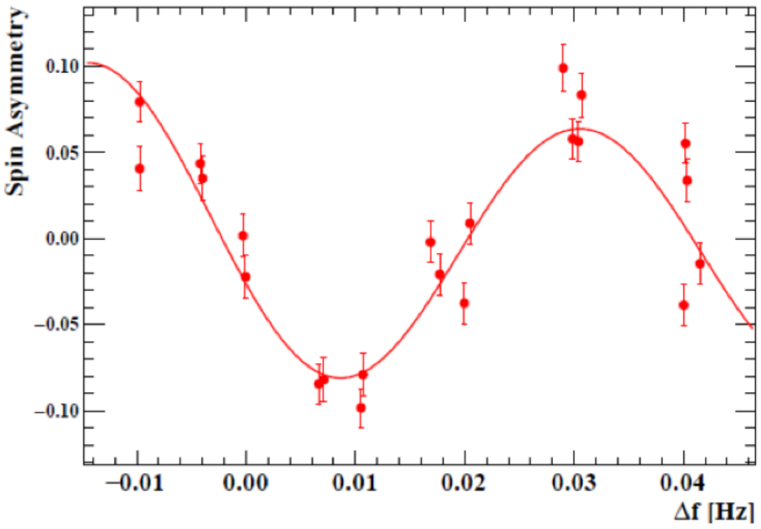

Figure 3.6: A Ramsey fringe pattern for a 20 second free precession time.

3.3.2 SNS nEDM

A new cryogenic nEDM experiment is currently being built at the Spallation Neutron Source (SNS) at Oak Ridge National Laboratory (ORNL) that aims to push the current limit of the nEDM statistical uncertainty to $2-3\times10^{-28}$ e cm [45]. This experiment will utilize ^{4}He to produce UCNs as well to serve as an insulating medium which will allow for an electric field that is much higher than all previous experiments.

The details of this experiment will be discussed in the following sections.

CHAPTER 4

SNS NEDM EXPERIMENT

4.1 Overview of Experiment

The SNS neutron EDM experiment will utilize several unique techniques in order to reach the desired sensitivity limit. Among these is the superthermal production of ultracold neutrons directly in the cell which will increase the density of the neutrons as compared to previous experiments. Another contributing factor will be the use of ^3He as both a spin analyzer and co-magnetometer. Both of these techniques will be described in the following sections.

4.2 Superthermal Production of UCNs

The UCNs are produced via downscattering of slow neutrons in superfluid ^4He [46, 41, 47]. Due to conservation of both energy and momentum, only neutrons that satisfy

$$E = \frac{\hbar k^2}{2m} \tag{4.1}$$

with momentum $\hbar k^*$ and energy $\hbar\omega$ will be downscattered into UCNs. Fig.4.1 shows the dispersion curves for free neutrons and superfluid ^4He. The intersection point of the two curves corresponds to the necessary energy and momentum of a free neutron to downscatter into a UCN via the emission of a phonon. Neutrons create phonons in the liquid helium which scatter the neutron to nearly at rest.

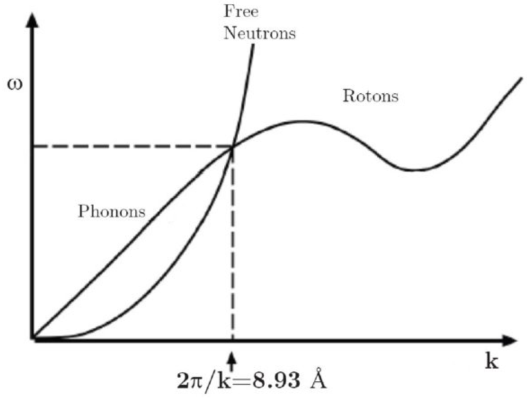

Figure 4.1: Free neutron and superfluid ^4He elementary dispersion curves.[39]

A neutron with momentum $\hbar k^*$ will come to rest via an emission of a single phonon. This will correspond to a neutron with a deBroglie wavelength of 8.93Å.

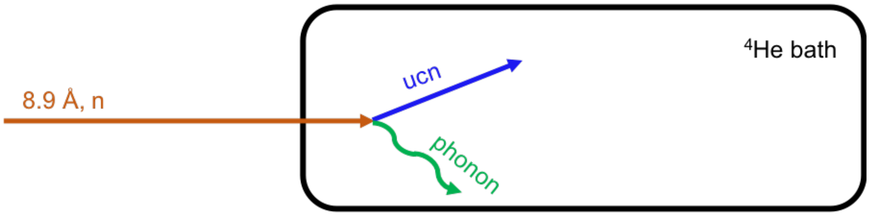

Figure 4.2: Schematic diagram of a cold neutron down scattering to an ultracold neutron in a bath of ^4He.

4.3 Helium 3 as a Spin Analyzer and Co-magnetometer

^3He in the measurement cells is used to monitor the neutron precession rate. Neutrons can be captured by ^3He and this absorption is highly spin dependent: neutrons are absorbed when the neutron spins are opposite to those of ^3He[1]. The absorption reaction is shown in Eq.4.2

$$^3He + n \rightarrow p +^3H + 764 \text{ keV}. \tag{4.2}$$

The energetic particles p and ^3H released in the reaction deposit their energy in the ^4He bath which causes the helium to scintillate in the extreme ultraviolet (EUV) region. EUV light does not pass through most materials, therefore the walls of the cell are coated in a material that will convert the EUV light into the visible region. This light can then be detected via photomultiplier tubes (PMTs).

By monitoring the scintillation rate, one can detect shifts in the Larmor precession frequency of the neutron. Because the neutron capture rate is dependent on the angle between the neutrons and ^3He polarizations, the scintillaion rate will vary as:

$$s(t) \propto 1 - \vec{P}_3 \cdot \vec{P}_n = 1 - P_3 P_n \cos(\theta_{3n}) \tag{4.3}$$

where $\vec{P}_3$ and $\vec{P}_n$ are the spin polarization vectors of the neutrons and ^3He respectively, and θ_{3n} is the angle between them and can be expressed in terms of $\theta_{3n} = (\gamma_n - \gamma_3)B_0 t = \omega_{3n} t$.

In the presence of a neutron EDM, θ_{3n} will change upon the reversal of the $\vec{E}$ field resulting in a change in the scintillation rate. We can now rewrite Eqs.3.1 and 3.2 as:

$$(\omega_3 - \omega_n)_{\uparrow\uparrow} = -(\gamma_3 - \gamma_n)B + \frac{2d_n E}{\hbar} \tag{4.4}$$

---

[1] The cross section for neutron absorption by ^3He is 11 kbarns when the spins of the two are antialigned and 59 barns when spins are aligned.

and

$$(\omega_3 - \omega_n)_{\uparrow\downarrow} = -(\gamma_3 - \gamma_n)B - \frac{2d_nE}{\hbar}. \tag{4.5}$$

By monitoring the scintillation rate, one can measure d_n.

$$d_n = \frac{[(\omega_3 - \omega_n)_{\uparrow\uparrow} - (\omega_3 - \omega_n)_{\uparrow\downarrow}]\hbar}{4E} = \frac{\hbar\Delta\omega_{3n}}{4E}. \tag{4.6}$$

The ^3He can also be used as a co-magnetometer to monitor the $|\vec{B}_0|$ inside of the cell. A set of SQUID[2] loops can be placed around the cell containing the neutrons and ^3He and used to measure the precession of the ^3He polarization. Because the ^3He electric dipole moment will be shielded by atomic electrons, its precession frequency will only depend on the magnetic field inside of the cell. Thus, any variation in the precession frequency of the ^3He will signal a change in the $|\vec{B}|$.

4.4 Dressed Spin Magnetometry

One method used to measure the Larmor precession frequency of the neutrons is critical dressing [41, 42] of the spins. In the presence of a constant magnetic field $\vec{B}_0$, the neutron and ^3He spins will precess at a Larmor frequency given by

$$\omega_i = \gamma_i B_0 \tag{4.7}$$

where $i = n$ for the neutrons and $i = 3$ for the ^3He. Because $\gamma_n \neq \gamma_3$, the spins will precess at different rates ($\omega_n \neq \omega_3$). By introducing an alternating magnetic field $\vec{B}_1$ oriented perpendicular to $\vec{B}_0$, the magnetic moment of each species can be modified, or "dressed", resulting in a change of the gyromagnetic ratio.

$$\gamma_d = \gamma_i J_0\left(\gamma_i \frac{B_1}{\omega_1}\right) = \gamma_i J_0\left(x\right) \tag{4.8}$$

where γ is the unperturbed gyromagnetic ratio, B_1 and ω_1 are the amplitude and frequency of the applied oscillating field, J_0 is the zeroth-order Bessel function and $x = \gamma_i \frac{B_1}{\omega_1}$. It is now possible to dress γ_i such that the neutrons and ^3He precess at the same rate.

$$\begin{gathered} \omega_3 = \omega_n \\ \gamma_3 J_0(x_3) = \gamma_n J_0(x_n) \end{gathered} \tag{4.9}$$

This will occur when $x_n \approx 1.22$[3] and is known as critical dressing. In the absence of an nEDM and under critical dressing, the scintillation rate will be constant as θ_{3n} remains unchanged during the measurement cycle. In the presence of an nEDM the

---

[2] Superconducting Quantum Interference Device

[3] Using $\gamma_3 = 1.1\gamma_n$, one can show that $\gamma_n J_0(x_n) = \gamma_3 J_0(\frac{\gamma_3}{\gamma_n})$ which has a first solution when $x \approx 1.22$. First, $\gamma_3 J_0(x_3) = \gamma_3 J_0(\gamma_3 \frac{B_1}{\omega_1}) = \gamma_3 J_0(1.1\gamma_n \frac{B_1}{\omega_1}) = \gamma_3 J_0(\frac{\gamma_3}{\gamma_n}\gamma_n \frac{B_1}{\omega_1})$. Thus, $\gamma_n J_0(x_n) = \gamma_3 J_0(\frac{\gamma_3}{\gamma_n} x_n)$.

application of an $\vec{E}$ field will result in a shift in the precession frequency and a drift in θ_{3n} with time:

$$\theta_{3n} = \omega_{3n} t = \frac{2[d_n J_0(x_d)]Et}{\hbar}. \tag{4.10}$$

By measuring the value of the dressing parameter x_d with respect to the electric field $\vec{E}$, the experiment will be sensitive to the nEDM. The benefit of this method is that by dressing the spins to precess at the same rate, the measurement is done without the effect of the DC $\vec{B}_0$ field and especially reduces the effect of temporal drifts in $\vec{B}_0$.

4.5 Overview of Measurement

The SNS nEDM experiment will use two rectangular storage cells in which polarized UCNs and ^3He are allowed to precess in parallel electric and magnetic fields. The precession frequencies of the UCN and ^3He will be measured in order to extract the neutron EDM. The measurement cycle is described below:

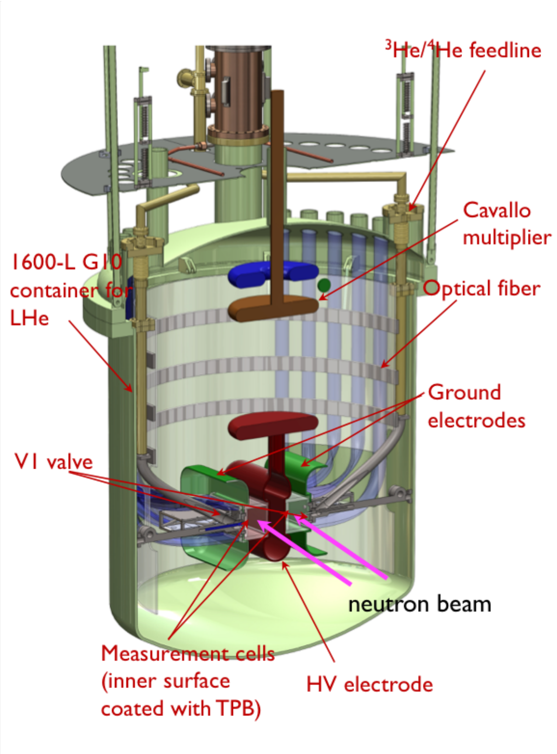

Figure 4.3: Diagram of the central detector system in the SNS nEDM experiment.

1. UCN are produced from a beam of 8.9 angstrom neutrons with their spins polarized along the direction of the holding field $\vec{B}_0$. The polarized ^3He atoms are introduced into the storage cells.
2. Using a $\pi/2$ pulse the spins of the UCN and ^3He are rotated such that they are perpendicular to the holding field.

3. The neutrons and ^3He are allowed to precess about the holding field.
4. The scintillation light that is produced in the liquid helium as a result of the capture of neutrons by ^3He is detected as a measure of the difference between the precession frequency of the neutron and ^3He spins. The precession frequency of the ^3He is measured via the SQUID pick up loops which serves as a monitor of $|\vec{B}_0|$. By reversing the direction of the electric field with respect to the magnetic field, the shift in frequency will indicate the presence of an nEDM.
5. Alternatively, the dressed spin method is used to make the nEDM measurement independent of the holding field $\vec{B}_0$. By dressing the spins, the neutrons and ^3He are dressed to precess at the same rate. The presence of an nEDM will result in the change of the scintillation rate.
6. The depolarized ^3He atoms are removed from the storage cells, the electric field is reversed and the process is repeated.

CHAPTER 5

MAGNETIC FIELD MONITORING

5.1 Systematic Effects Due to Non-Uniformities in the Magnetic Field

Because the SNS neutron EDM experiment aims to reach such a small level of sensitivity, it is important to suppress systematic effects that may arise in the experiment, especially ones that can be of the order of the nEDM signal. In particular, false neutron EDM effects can arise from geometric phases [48] which will be discussed in detail in the following section.

5.1.1 Geometric Phase

A large concern to any nEDM experiment is the existence of systematic effects that can mimic a false nEDM signal. It is very difficult experimentally to realize a purely uniform magnetic field, and field gradients are usually present in the measurement cells. The presence of these gradients, along with motional magnetic fields, causes the neutrons to acquire a phase that results in the shift of the Larmor precession frequency, which can lead to such a false signal.

For neutrons moving in a static but non uniform magnetic field, the direction of this field in the reference frame of the neutrons will change which leads to the geometric phase effects. To illustrate how the geometric phase can lead to a false nEDM signal, one can consider the case of a classical spin in a uniform magnetic field confined to a cylindrical trap (Fig.5.1).

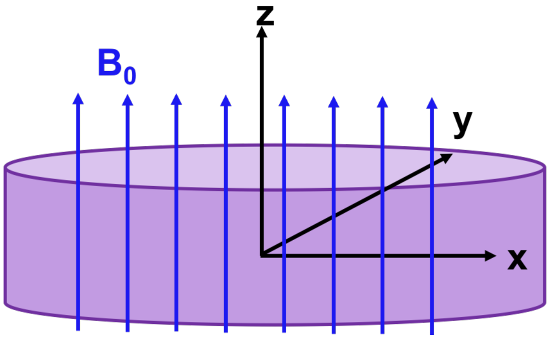

Figure 5.1: A cylindrical cell with a unifom magnetic field along the z-axis.

Suppose that within the container, there exists a constant and uniform magnetic field along the z-axis:

$$\overrightarrow{B_0} = B_0\hat{z}. \tag{5.1}$$

The spin will precess about this field with a Larmor precession frequency

$$\overrightarrow{\omega_L} = \overrightarrow{\omega_0} = -\gamma \overrightarrow{B_0}. \tag{5.2}$$

Suppose, now, that we view this precession in the reference frame that is rotating in the frame at an angular speed ω_r. The Larmor precession frequency will now be shifted away from ω_0 and result in a relative precession frequency given by

$$\Delta\vec{\omega} = \overrightarrow{\omega_0} - \overrightarrow{\omega_r} = -\gamma\Big(\overrightarrow{B_0} - \frac{\overrightarrow{\omega_r}}{\gamma}\Big) = -\gamma \overrightarrow{B}_{\text{eff}}. \tag{5.3}$$

Now, suppose that in addition to the uniform magnetic field, there is another magnetic field in the xy-plane rotating at an angular speed ω_r about $\hat{z}$. Thus, the superimposed magnetic field is of the form

$$\vec{B} = \vec{B}_{xy} + \vec{B_0}. \tag{5.4}$$

It is useful to consider this problem in a reference frame that rotates at a frequency $\vec{\omega}_{rot} = -\omega_{rot}\vec{z}$ resulting in a time-independent field in this frame of reference

$$\vec{B_s} = B_{xy}\hat{x}_{rot} + B_{\text{eff}}\hat{z} = B_{xy}\hat{x}_{rot} + \Big(B_{0z} - \frac{\omega_{rot}}{\gamma}\Big)\hat{z}. \tag{5.5}$$

In this reference frame, the spin will precess about $\vec{B_s}$ at a frequency

$$|\vec{\omega_s}| = \gamma|\vec{B_s}| = \gamma\sqrt{B_{xy}^2 + \Big(B_{0z} - \frac{\omega_{rot}}{\gamma}\Big)^2}. \tag{5.6}$$

Thus, the shift in the precession frequency due to the rotating $\vec{B_{xy}}$ field is given by

$$\begin{aligned}
\Delta\omega &= \omega_s - \omega_L \\
&= \gamma\sqrt{B_{xy}^2 + \Big(B_{0z} - \frac{\omega_r}{\gamma}\Big)^2} - \gamma\Big(B_{0z} - \frac{\omega_r}{\gamma}\Big) \\
&= \sqrt{\omega_{xy}^2 + (\omega_0 - \omega_{rot})^2} - (\omega_0 - \omega_{rot}) \\
&= (\omega_0 - \omega_{rot})\sqrt{1 + \frac{\omega_{xy}^2}{(\omega_0 - \omega_{rot})^2}} - (\omega_0 - \omega_{rot}).
\end{aligned} \tag{5.7}$$

To first order of $\omega_{xy} \ll \omega_0$, Eq.5.7 becomes

$$\begin{aligned}
\Delta\omega &= \frac{\omega_{xy}^2}{2(\omega_0 - \omega_r)} \\
&= \frac{\gamma^2 B_{xy}^2}{2(\omega_0 - \omega_{rot})}.
\end{aligned} \tag{5.8}$$

One can now consider the frequency shift due to non-uniformities in $\vec{B_0} = B_0\hat{z}$, specifically a vertical gradient $\frac{\partial B_{0z}}{\partial z}$, and motional magnetic fields present within the measurement cell.

Such a vertical gradient will produce a field in the xy-plane of the form[1]

$$\overrightarrow{B_{0xy}} = -\left(\frac{\partial B_{0z}}{\partial z}\right)\frac{\vec{r}}{2}. \tag{5.9}$$

According to special relativity, a magnetic field will be induced in the frame of the neutron due to its motion within an electric field, $\vec{E}$ (Fig.5.2).

$$\vec{B_v} = \frac{\vec{E}\times\vec{v}}{c^2}. \tag{5.10}$$

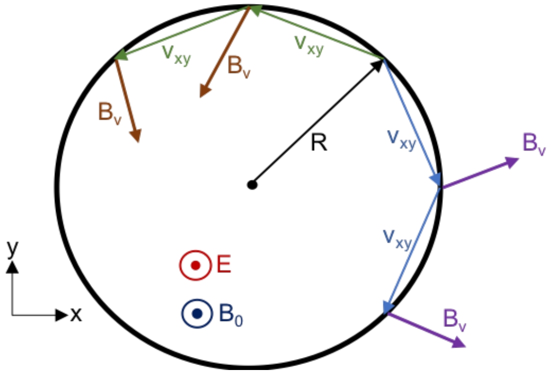

Figure 5.2: Illustration of induced motional magnetic field, $\vec{B_v}$, for a particle undergoing specular collisions in the xy-plane.

Thus, in the reference frame of the neutrons, the total field becomes

$$\begin{aligned}\vec{B_n} &= \vec{B_v} + \vec{B_{0xy}}\\ \vec{B_n} &= -\left(\frac{\partial B_{0z}}{\partial z}\right)\frac{\vec{r}}{2} + \frac{\vec{E}\times\vec{v}}{c^2}.\end{aligned} \tag{5.11}$$

Substituting Eq.5.11 in Eq.5.8, we can express the frequency shift in terms of the electric field $\vec{E}$:

$$\Delta\omega = \frac{\gamma^2\left(\left(\frac{\partial B_{0z}}{\partial z}\right)\frac{\vec{r}}{2} + \frac{\vec{E}\times\vec{v}}{c^2}\right)^2}{2(\omega_0-\omega_r)}. \tag{5.12}$$

The geometric phase now contains a cross term that is linear in $\vec{E}$ that will not average to zero upon consideration of neutrons rotating in both directions and will contribute to the precession frequency. The frequency difference now becomes[2]

$$\Delta\omega_{\uparrow\uparrow} - \Delta\omega_{\uparrow\downarrow} = -2\gamma^2\left(\frac{R}{2}\frac{\partial B_{0z}}{\partial z}\right)\frac{v_{xy}E}{c^2}\frac{|\omega_r|}{(\omega_0^2-\omega_r^2)}. \tag{5.13}$$

For UCNs, $\frac{\omega_r}{\omega_0} \ll 1$ and Eq. 5.13 becomes

$$\Delta\omega_{\uparrow\uparrow} - \Delta\omega_{\uparrow\downarrow} = \left(\frac{\partial B_{0z}/\partial z}{B_{0z}^2}\right)\frac{v_{xy}^2 E}{2c^2}\left[1-\frac{\omega_r^2}{\omega_0^2}\right]^{-1} \tag{5.14}$$

---

[1] Note here that we are assuming cylindrical symmetry.

[2] Here $|\omega_r| = \frac{|v_{xy}|}{R}$

which corresponds to a false nEDM of [48]:

$$d_{f,n} = -\frac{\hbar}{4}\left(\frac{\partial B_{0z}/\partial z}{B_{0z}^2}\right)\frac{v_{xy}^2}{c^2}\left[1-\frac{\omega_r^2}{\omega_0^2}\right]^{-1}. \tag{5.15}$$

For values of $\frac{\partial B_{0z}}{\partial z} = 10\frac{\mathrm{pT}}{\mathrm{cm}}$, $B_{0z} = 3\mu\mathrm{T}$, and $v_{xy} = 2.4\frac{\mathrm{m}}{\mathrm{s}}$, the resulting false nEDM is -1.17×10^{-28} e cm. Because this effect is on the order of the expected nEDM signal, it is important to control the magnetic field gradients in the experiment.

Because the experiment relies on the measurement of the precession frequency of ^3He, it is important to consider the geometric phase effect on the ^3He. Because the ^3He resides in the bath of ^4He along with the neutrons, it will experience essentially the same $\vec{B}$ and $\vec{E}$ fields as the UCNs and will be subject to the geometric phase effect. As has been shown by Golub et al. [49], the false EDM effect for ^3He can be reduced by an appropriate choice of operating temperature due to the dependence on the collision rate between ^3He and phonons in the ^4He superfluid bath [50]. Thus, by varying the temperature, the experiment can probe the temperature dependence of the ^3He geometric phase false EDM effect, which will provide for a powerful validation of the theory. Further, under certain operating conditions, the false EDM effect of the ^3He can be significantly reduced [45, 51].

5.1.2 Spin Relaxation

Another unwanted effect that can arise from magnetic field non-uniformities is the depolarization of the neutrons during the measurement cycle [52]. Suppose that the neutrons, which are confined to a measurement cell, are initially polarized such that all of the spins are aligned perpendicular to the holding field $\vec{B}_0$[3]. The spins will then precess about $\vec{B}_0$. If the field within the measurement cell is not uniform, as the neutrons move about the cells, they will experience different magnetic fields based on their position within the cell. This will cause the spins to precess at different rates and point along different directions. This, in turn, will result in the decrease of the ensemble polarization. If the neutron spins depolarize quickly, the free precession measurement time will be short. Because the sensitivity of the measurement relies on a long precession measurement time (3.6), it is important to maximize the spin relaxation time. This spin relaxation time is known as the transverse spin relaxation T_2 and can be expressed using the McGregor formalism [53] in terms of the magnetic field gradients

$$\frac{1}{T_2} = \frac{L^4\gamma^2\left|\frac{\partial B_0}{\partial z}\right|^2}{120D} + \frac{1}{2T_1} \tag{5.16}$$

where D is the diffusion coefficient, L the length of the storage cell and T_1 is the longitudinal spin relaxation which represents the spins oriented along $\vec{B}_0$ [53].

$$\frac{1}{T_1} = \frac{\gamma^2}{2}\left(\left|\frac{\partial B_0}{\partial x}\right|^2 + \left|\frac{\partial B_0}{\partial y}\right|^2\right)\frac{2(\frac{k_B T}{M})\tau_c}{\omega^2(1+\omega^2\tau_c^2)} \tag{5.17}$$

---

[3] In this case, $\vec{S}\cdot\vec{B}_0 = 0$.

Here M is the mass of the neutron, k_B is the Boltzmann constant, τ_c is the time between wall collisions and T is the temperature.

5.1.3 Uniformity Requirement of the Magnetic Field

5.2 Overview of the Field Reconstruction Method

While one cannot measure the magnetic field within the experimental region directly due to geometric constraints of the experimental apparatus, it is often possible to measure the field on some surface external to the region of interest, as illustrated in Fig.5.3.

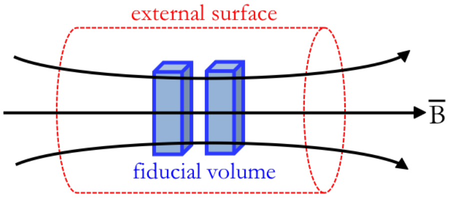

Figure 5.3: Schematic illustration of the boundary value reconstruction concept.

In the case that there are no sources of currents or magnetization enclosed within the volume interior to the surface, i.e. $\vec{J} = 0$ and $\vec{M} = 0$, it then follows that the internal magnetic field satisfies the Laplace equation, $\vec{\nabla}^2\vec{B} = 0$. Furthermore, one can also define a magnetic scalar potential, $\Phi_M(\vec{x})$, which will also satisfy the Laplace equation since $\vec{\nabla}\cdot\vec{B} = 0$. The solutions to the Laplace equation are well known and can be expressed in terms of a multipole expansion of the form [54]

$$\Phi(r,\theta,\phi) = \sum_{\ell=0}^{\infty}\sum_{m=0}^{+\ell} r^{\ell} P_{\ell}^{m}(\cos\theta)[a_{\ell m}\cos m\phi + b_{\ell m}\sin m\phi] \tag{5.18}$$

where $P_\ell^m(\cos\theta)$ are the Legendre Polynomials. It then follows from $\vec{B} = -\vec{\nabla}\Phi_M$ that the magnetic field in spherical components is of the form [55]:

$$\begin{aligned} B_r(\vec{x}) &= -\frac{1}{r}\sum_{\ell,m}[\ell C_{\ell,m}(\vec{x})a_{\ell,m} + \ell S_{\ell,m}(\vec{x})b_{\ell,m}] \\ B_\theta(\vec{x}) &= -\frac{1}{\sin\theta}\sum_{\ell,m}[\Delta_{\ell,m}(\vec{x})a_{\ell,m} + \Lambda_{\ell,m}(\vec{x})b_{\ell,m}] \\ B_\phi(\vec{x}) &= -\frac{1}{r\sin\theta}\sum_{\ell,m}[mC_{\ell,m}(\vec{x})b_{\ell,m} + mS_{\ell,m}(\vec{x})a_{\ell,m}] \end{aligned} \tag{5.19}$$

where $C_{\ell,m}(\vec{x})$, $S_{\ell,m}(\vec{x})$, $\Delta_{\ell,m}(\vec{x})$ and $\Lambda_{\ell,m}(\vec{x})$ are known basis functions of the form:

$$\begin{aligned} C_{\ell m}(\vec{x}) &= r^{\ell} P_{\ell}^{m} \cos\theta \cos m\phi \\ S_{\ell m}(\vec{x}) &= r^{\ell} P_{\ell}^{m} \cos\theta \sin m\phi \\ \Delta_{\ell m}(\vec{x}) &= -\frac{\ell}{r} C_{\ell m}(\vec{x}) \cos\theta - (\ell+m) C_{\ell-1,m}(\vec{x}) \\ \Lambda_{\ell m}(\vec{x}) &= -\frac{\ell}{r} S_{\ell m}(\vec{x}) \cos\theta - (\ell+m) S_{\ell-1,m}(\vec{x}) \end{aligned} \tag{5.20}$$

and $a_{\ell,m}$ and $b_{\ell,m}$ are arbitrary expansion coefficients which depend upon the intrinsic properties of the field. Thus, by measuring the field components B_i on the external surface at some N different locations, it is possible to determine the unknown expansion coefficients $a_{\ell,m}$ and $b_{\ell,m}$. This permits the reconstruction of the magnetic field at every point in the interior volume. We have chosen to preform this basis function analysis in rectangular coordinates and the coordinate transformation of the basis functions is shown in Appendix B of Ref.[55][4].

The question then arises: at how many locations does one need to measure the field components on the external surface in order to accurately reconstruct the field? First, let us rewrite Eqs.5.19 in the following way:

$$B_i = \sum_n a_n F_n(x,y,z) \tag{5.21}$$

where B_i represents the field measurement at some location on the surface, F_n the known basis functions and a_n the unknown expansion coefficients that are characteristic of the field. Thus, for every expansion coefficient and basis function, there needs to be an external measurement. If one is able to make an infinite number of measurements of the field components on the external surface, one could reconstruct the internal field with maximal accuracy. Since this is not practical (or even feasible) in most experiments, the number of sensors, and thus basis functions, is determined by the profile of the magnetic field in the region of interest.

One might now ask, where must these exterior measurements be made in order to achieve maximal accuracy of the reconstruction of the interior magnetic field? In order to determine these locations, one must first find where the basis functions for each term in the multipole expansion are maximal in magnitude. A simple way to

---

[4] Note that Eq. B.2 should read:

$$\Phi_M(\vec{x}) = \sum_{\ell,m} (\rho^2+z^2)^{\ell/2} P_\ell^m\left(\frac{z}{\sqrt{\rho^2+z^2}}\right) \times \left[a_{\ell,m} \sum_{k=0}^{m/2} (-1)^k \binom{m}{2k} \left(\frac{y}{\rho}\right)^{2k} \left(\frac{x}{\rho}\right)^{m-2k} \right. \\ \left. + b_{\ell,m} \sum_{k=0}^{(m-1)/2} (-1)^k \binom{m}{2k+1} \left(\frac{y}{\rho}\right)^{2k+1} \left(\frac{x}{\rho}\right)^{m-2k-1}\right].$$

achieve this is to project the basis functions onto the external measurement surface in order to determine the locations of the maxima [55]. The field sensors should then be located at or near these maxima, thus maximizing the sensitivity of the external measurements to the terms in the multipole expansion that are characteristic of the properties of the magnetic field within the region of interest. Table 5.1 lists the first few basis functions in the multipole expansion of $B_x(\vec{x})$ in rectangular coordinates and Fig.5.4 shows examples for such projections of four different basis functions onto a cylindrical measurement surface.

Table 5.1: Basis functions for $B_x(\vec{x})$ in rectangular coordinates

Coefficient	Basis Function	Coefficient	Basis Function
$\mathbf{a}_{1,1}$	-1	$\mathbf{b}_{1,1}$	0
$\mathbf{a}_{2,0}$	$-x$	$\mathbf{b}_{2,0}$	0
$\mathbf{a}_{2,1}$	$-3z$	$\mathbf{b}_{2,1}$	0
$\mathbf{a}_{2,2}$	$6x$	$\mathbf{b}_{2,2}$	6y
$\mathbf{a}_{3,0}$	$-3xz$	$\mathbf{b}_{3,0}$	0
$\mathbf{a}_{3,1}$	$\frac{3}{2}(3x^2 + y^2 - 4z^2)$	$\mathbf{b}_{3,1}$	3xy
$\mathbf{a}_{3,2}$	$30xz$	$\mathbf{b}_{3,2}$	30yz
$\mathbf{a}_{3,3}$	$45(-x^2 + y^2)$	$\mathbf{b}_{3,3}$	-90xy
$\mathbf{a}_{4,0}$	$\frac{3}{2}x(x^2 + y^2 - 4z^2)$	$\mathbf{b}_{4,0}$	0
$\vdots$	$\vdots$	$\vdots$	$\vdots$

In addition, the projection method allows for the discrimination between contributions from different basis functions. This can be demonstrated with the following example. Suppose we have two functions, $f_1(\vec{x}) = x^2$ and $f_2(\vec{x}) = z^2$, whose projections onto a cylindrical surface are shown in Figs.5.5a and 5.5b, respectively.

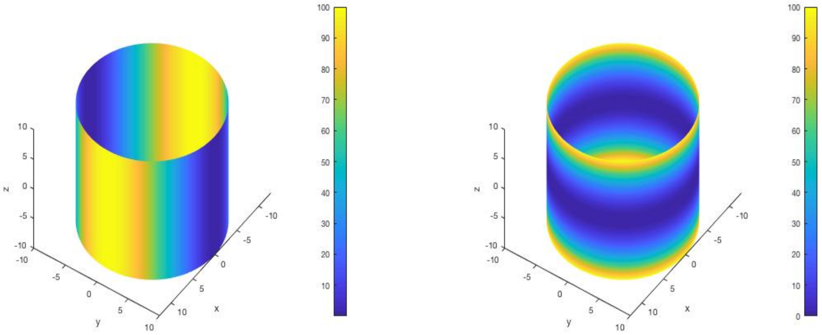

(a) Solution of $f_1(\vec{x}) = x^2$ on a cylindrical surface.

(b) Solution of $f_2(\vec{x}) = z^2$ on a cylindrical surface.

Figure 5.5: Example of discriminating between two basis functions.

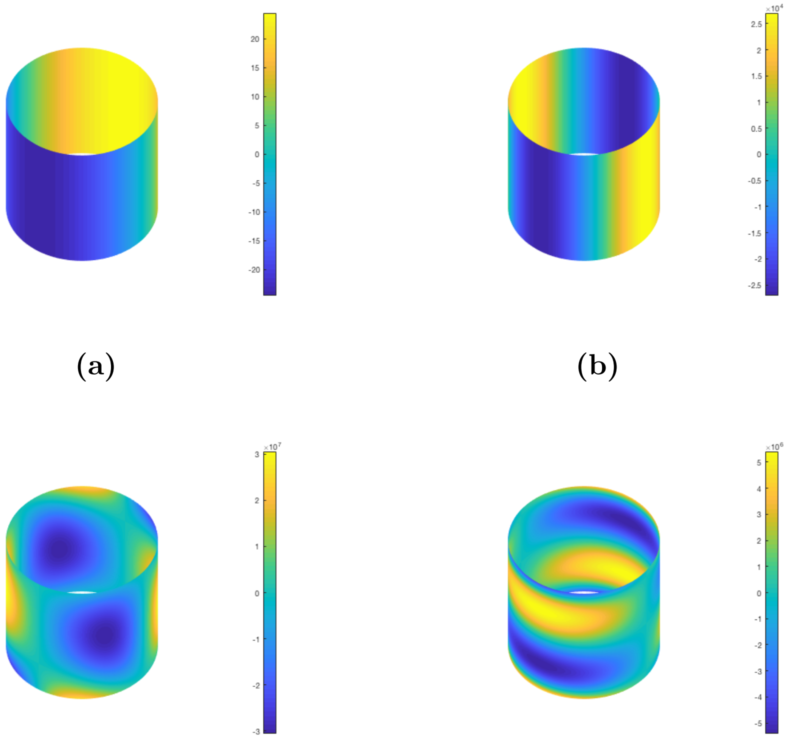

(a) **(b)**

(c) **(d)**

Figure 5.4: Examples of solutions of basis functions on a cylindrical surface for (a) $a_{2,0}$ of $B_x(\vec{x})$, (b) $a_{3,3}$ of $B_x(\vec{x})$, (c) $a_{5,2}$ of $B_y(\vec{x})$ and (d) $a_{5,1}$ of $B_z(\vec{x})$.

It is clear that if the field is measured by a sensor located at $z = 10, \phi = \frac{\pi}{2}$, then it is impossible to know if this contribution is coming from $f_1(\vec{x})$ or $f_2(\vec{x})$. However, if we also make a measurement at $z = 0, \phi = \frac{\pi}{2}$, where $f_1(\vec{x})$ has a maximum and $f_2(\vec{x}) = 0$, we can discriminate between these two functions.

5.3 Studies of Prototype

5.3.1 Characterization of Magnetic Field Sensors

It is important that the devices used for measuring the magnetic field not only provide an accurate measurement of the field but also not interfere with the magnetic environment. Thus it is essential to study and characterize the sensors being used.

Bartington Mag F single axis cryogenic compatible fluxgate magnetometers were chosen for the sensor array.

The fluxgates are made of two highly permeable cores that are brought in and out of saturation by supplying an AC signal to the excitation coils. When they reach saturation, the permeability of the cores decrease dramatically which gives rise to a signal in the secondary pick up coil. In a zero field environment the signals generated

Figure 5.6: Bartington Mag F single axis cryogenic compatible fluxgate magnetometers and the Mag-01H electronic readout unit.

by each core cancel out. If there is an external field, one core will reach saturation before the other giving rise to an induced voltage in the pick up coil. A compensation current that is proportional to the measured field is then generated in the pickup coil. The external magnetic field is determined by measuring the amplitude of the current in the pick up coil.

5.3.1.1 Offsets

In a perfect world, the measurement obtained by a field sensor will be exactly the field produced by the field coils. However, this is not always the case in the real world! There can exist inherent offsets in the field sensors that arise from various sources such as the electronics used to drive the probes or the materials they are made from. Thus, it is imperative to have precise knowledge of these offsets.

One way to determine the offset of a field sensor is to compare the measurement of a constant external field with the probe aligned with the field and anti-aligned as shown in Fig.5.7.

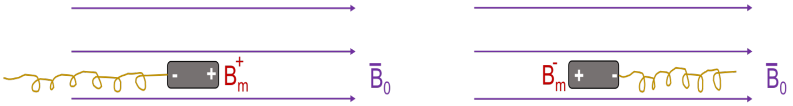

(a) B^+ **(b)** B^-

Figure 5.7: Offset Measurement

For the sensor aligned with the external field, the measurement will be comprised of the true B_0 field and the sensor offset Δ:

$$B_m^+ = B_0 + \Delta \tag{5.22}$$

Similarly, for the sensor anti-aligned with the external field:

$$B_m^- = -B_0 + \Delta \tag{5.23}$$

One can now extract the offset of the sensor:

$$\Delta = \frac{B_m^+ + B_m^-}{2} \tag{5.24}$$

In order to get the most accurate measurement of the offsets of each sensor, the measurements are performed in a small magnetic field in order to minimize any errors that can arise from the drifting or variations of the magnetic field. The experimental setup is shown in Fig.5.8.

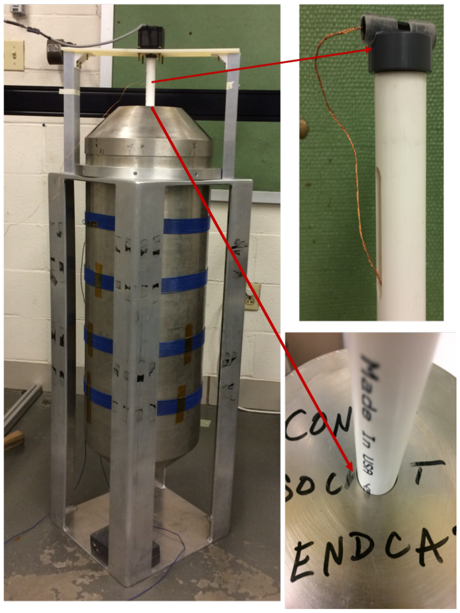

Figure 5.8: Experimental setup to measure the offsets of the Mag F sensors at room temperature.

The offset measurements are performed inside of a mu-metal shield (referred to as the “rocket”) with a set of external degaussing coils which allow for a background magnetic field $\mathcal{O}(4\text{ nT})$. The sensor is attached to a polycarbonate holder which is then connected to a PVC pipe 0.5” in diameter and 25” in length. The pipe passes into the rocket through a mu-metal lid with a pass-through hole just big enough for the probe to fit. The tight fit between the lid and PVC pipe allows for the shielding of any fields that may otherwise leak in through any available gaps. The rotational motion of the probe is controlled via a NEMA 23 single shaft, bipolar stepper motor with an angular resolution of 1.8 degrees. Field measurements are taken at 0 and 180 degrees for 5 seconds in each orientation. During the field measurements, the motor is powered down and unplugged from its power source to prevent contamination of the magnetic field. The offset is then extracted from the data. Figure 5.9 shows the offset measurement for one sensor measured at room temperature during the course of one night.

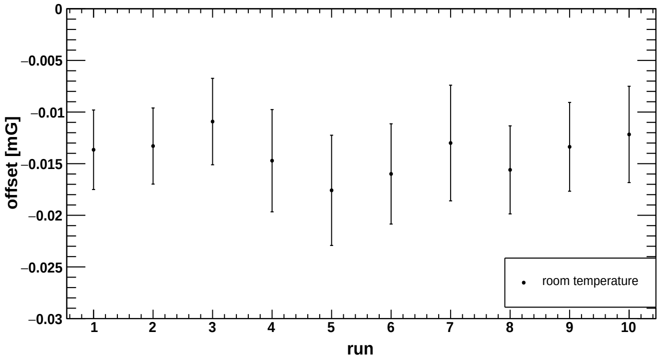

Figure 5.9: Offset measurements for a single probe at room temperature measured over the course of a single night.

Because the SNS nEDM experiment will be done at ~ 0.5K and the probe array will be at a temperature of ~ 4K, the offset measurements were repeated in liquid nitrogen (LN) (and, eventually, liquid helium). The sensors are made of two ferromagnetic cores wound by the excitation and feedback coil wires, thus the offsets may change due to thermal contraction of the materials. For these measurements a foam dewar was filled with LN and placed within the mu-metal rocket. The probe is then submerged in the LN and the offset measurement procedure repeated. The setup for these measurements is shown in Fig.5.10.

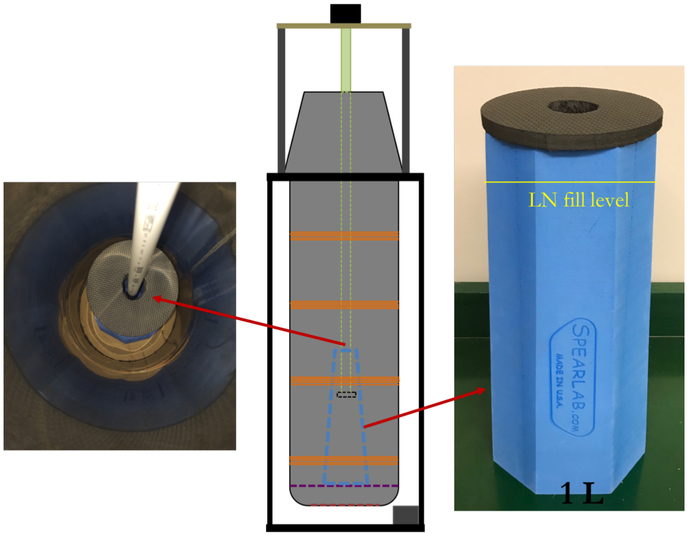

Figure 5.10: Experimental setup to measure the offsets of the Mag F sensors in liquid nitrogen.

The offsets of three different sensors measured in liquid nitrogen over the course of three nights is shown in Fig.5.11. It is important to note that the offset varies significantly for certain sensors over the course of several different measurement cycles. This can have potential impact on the results of the field reconstruction and will be discussed in Section 5.4.3.1. We also made measurements (Fig.5.12) of the temperature dependence of the offsets. For these measurements the probes were first submerged into the liquid nitrogen and the probe offset were measured as the liquid nitrogen boiled off. This allows us to calibrate the offsets of the probes in different temperature conditions.

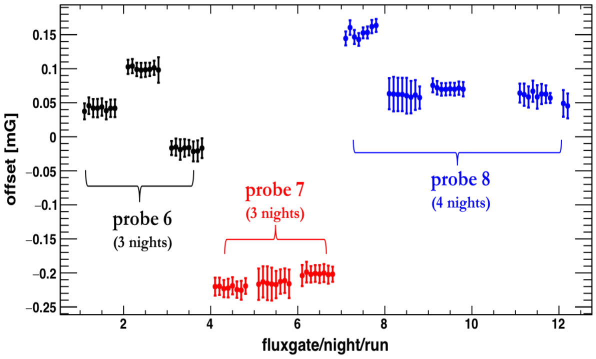

Figure 5.11: Offset measurements for three independent probes measured during the course of three different nights. These measurements were done with each of the probes submerged in liquid nitrogen.

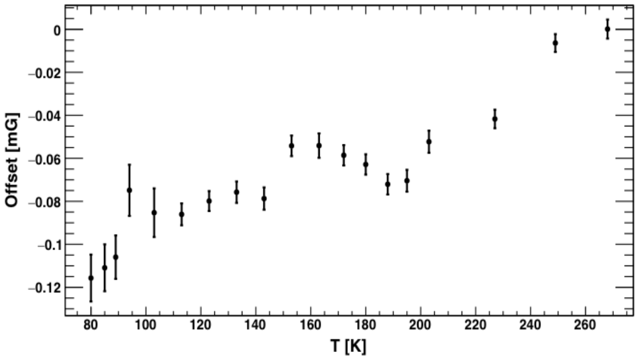

Figure 5.12: Temperature dependence of the offset of a single probe.

5.3.1.2 Gradients produced by probes

When a sensor is powered off, due to its ferromagnetic core, it will act as a dipole which will introduce gradients into the experimental region of interest. Because it is important to minimize any magnetic field non-uniformities it is vital to know the gradients that are produced by the sensors themselves.

The gradient measurements are performed inside of the mu-metal rocket using an active "observer" fluxgate magnetometer to measure the background magnetic field and a powered off "dummy" sensor. The dummy sensor is moved toward the active sensor via a triple axis field mapper and the background field recorded. One can fit the data and extract the gradient produced by the sensor at various locations. The experimental setup (Fig.5.13) is enclosed by a set of Helmholtz coils that produce a constant magnetic field along the axis of the rocket in order to prevent changes in the magnetization of the dummy sensor that can arise from variations in the background field of the rocket.

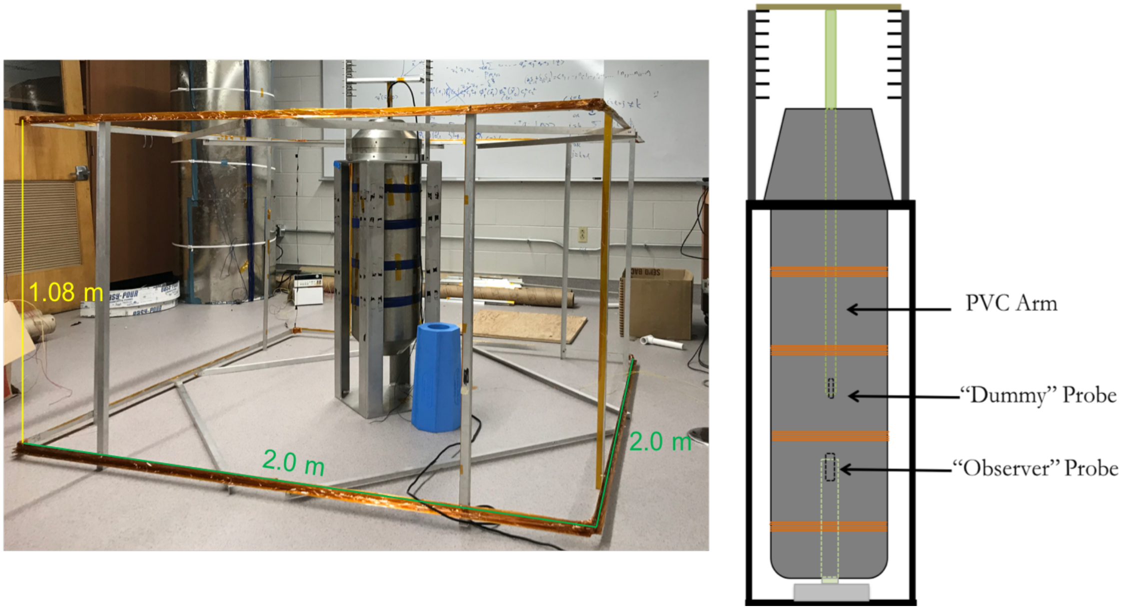

Figure 5.13: Experimental setup to measure gradients produced by Mag F sensors.

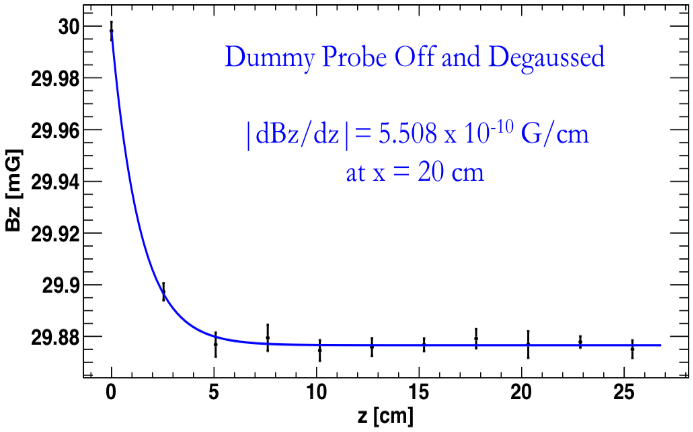

Figure 5.14: Gradient produced by a single sensor at a point 20 cm away.

Based on the results shown in Fig.5.14, the gradients produced by the probes themselves are not be large enough to interfere with the experimental measurements.

5.3.2 12 Probe Array

The first prototype was designed to be a cylindrical-type support structure that holds 12 single-axis cryogenic compatible fluxgate magnetometer probes. The structure is 25.4 cm in radius and 71.12 cm in length. The positions of the probes were determined using the optimization method described in Section 5.2 of this document. The positions were chosen such that the sensitivity to the basis functions was maximized and included the ability to distinguish the basis functions from one another. The array structure and sensor placements are shown in Table 5.2 and Fig.5.15. This design was informed by previous work done using a small scale prototype consisting of 12 lower-accuracy Stefan Mayer room temperature magnetic field sensors[56].

Location Number	ϕ	z (m)
1	0	0.25
2	$\pi/2$	-0.25
3	$\pi/2$	0.0
4	$\pi/2$	0.25
5	$3\pi/4$	-0.25
6	$3\pi/4$	0.0
7	π	-0.25
8	$3\pi/2$	0.0
9	$3\pi/2$	0.25
10	$7\pi/4$	-0.25
11	$7\pi/4$	0.0
12	$7\pi/4$	0.25

Table 5.2: Sensor Locations

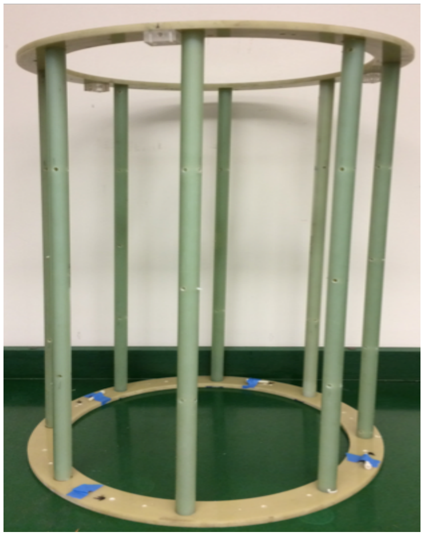

Figure 5.15: Prototype Array

The boundary values are measured using 12 Bartington Mag-F fluxgate magnetometer sensors. The sensors are connected to a single Mag-01 H electronic readout unit via a mechanical rotary switching box (Fig.5.16). The analog output of the Mag-01 H unit is read into an Agilent 34411A Digital Multimeter.

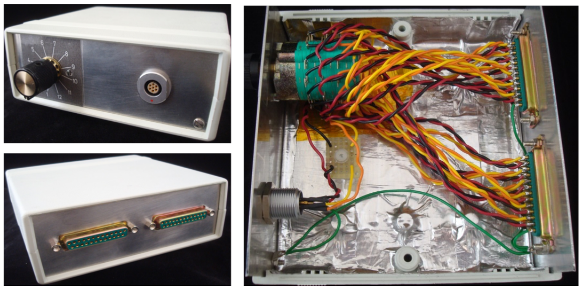

Figure 5.16: Probe switching system.

The first generation prototype was tested using the $\frac{1}{3}$ scale apparatus setup at Caltech. The measurement array was calibrated at room temperature in a magnetic field produced by a set of Helmholtz coils. The result of the field reconstruction using our method was compared to the field map data taken along the axis of the array using a triple axis probe. The reconstructed linear gradient was found to be in good agreement with the direct measurement (Fig.5.17b).

Following the preliminary testing of the prototype in the external Helmholtz coils, the sensor array was used to attempt a field gradient reconstruction of the $\cos\theta$ B_0 coil in the 1/3 scale apparatus. The sensor array was locked to the B_0 coil via nylon lock

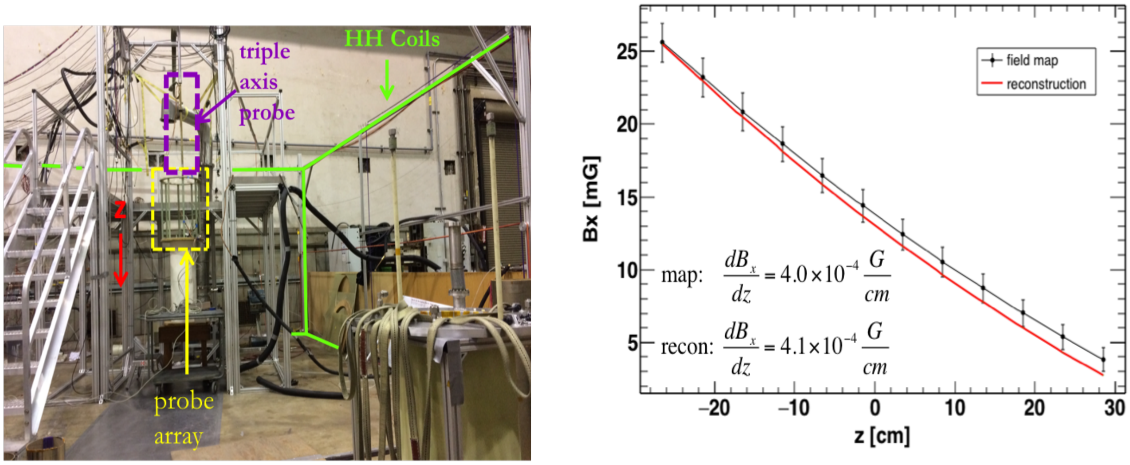

(a) Experimental setup at Caltech.

(b) Reconstructed field profile of B_x along z-axis.

Figure 5.17: Experimental setup and results of reconstruction test performed at room temperature.

screws and loaded into the inner vacuum chamber (IVC) along with Pb shielding. The IVC was then loaded into the outer vacuum chamber (OVC).

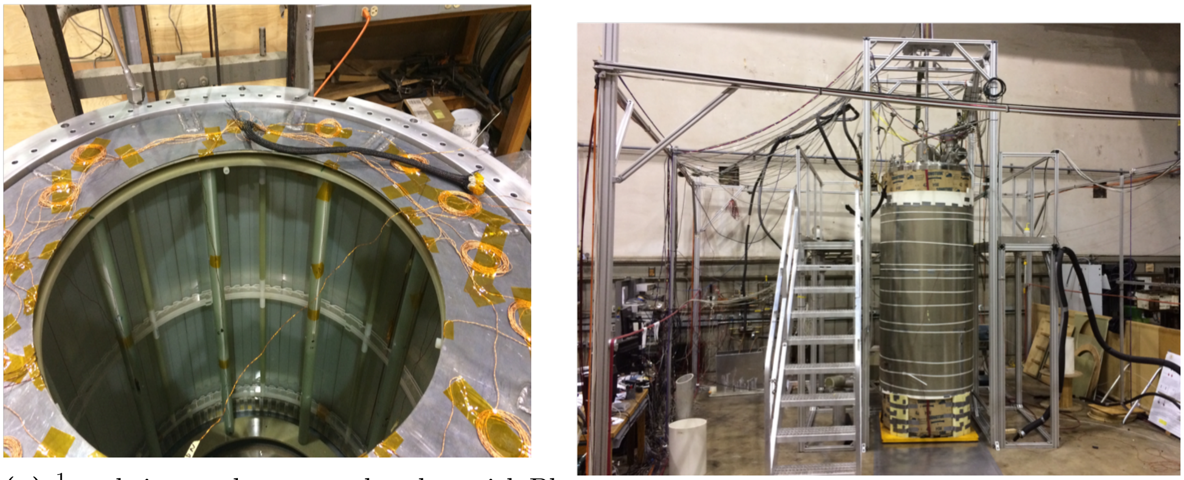

(a) $\frac{1}{3}$ scale internal vacuum chamber with Pb endcaps, $\cos\theta B_0$ coil, and 12 sensor array.

(b) $\frac{1}{3}$ scale outer vacuum chamber.

Figure 5.18: Third scale experimental setup at Caltech.

The data were taken both at room and liquid He temperatures in a holding field of ∼100 mG. The boundary values were measured successively using the switching box and field reconstructions were performed. The result of the room temperature measurement is shown in Fig.5.19.

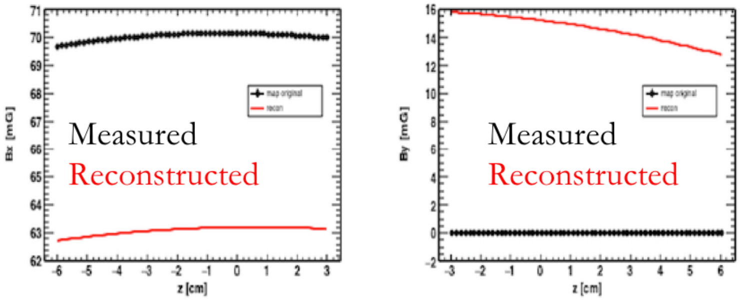

Figure 5.19: Result of reconstruction for B_x and B_y along the axis of the B_0 coil

It is clear from the results that we were unable to reconstruct the measured field. Eliminating errors that could arise from the position, orientation and drifting offset of the sensors, we had to reevaluate the design of the array. A Python simulation of the field profile of a $\cos\theta$ coil is shown in Fig.5.20 where the red lines indicate the location of the sensors of our array. It is clear that the field within the region interior to the probe array is of at least $\mathcal{O}(x^4)$. This requires a fourth order polynomial function to accurately reconstruct the field. Because the first generation prototype array consists of 12 sensors, we can only access the $\ell = 1$ and $\ell = 2$ basis functions, which only allows a reconstruction of a second order polynomial.

Thus, in order to accurately reconstruct the field within the experimental cells, we need to either decrease the radius of the array or increase the number of sensors being used. The former is not a viable option due to the design constraints of the experimental apparatus. Thus, we have designed a sensor array with an increased number of sensors as will be presented in Section 5.4.

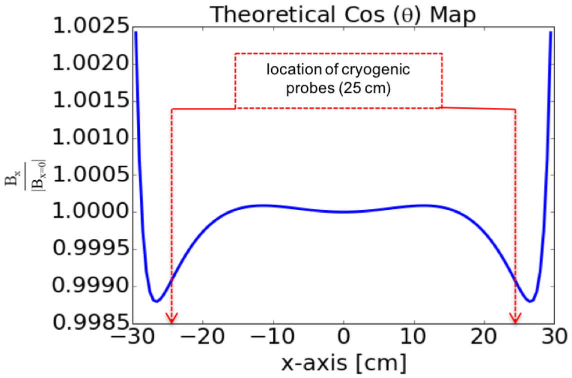

Figure 5.20: $\cos\theta$ coil theoretical field profile.

5.4 39 Sensor Array

5.4.1 Sensor Geometry

Based on the results of the previous prototype, a new sensor array has been designed that will be able to reconstruct the field profile within the cells to a high degree of

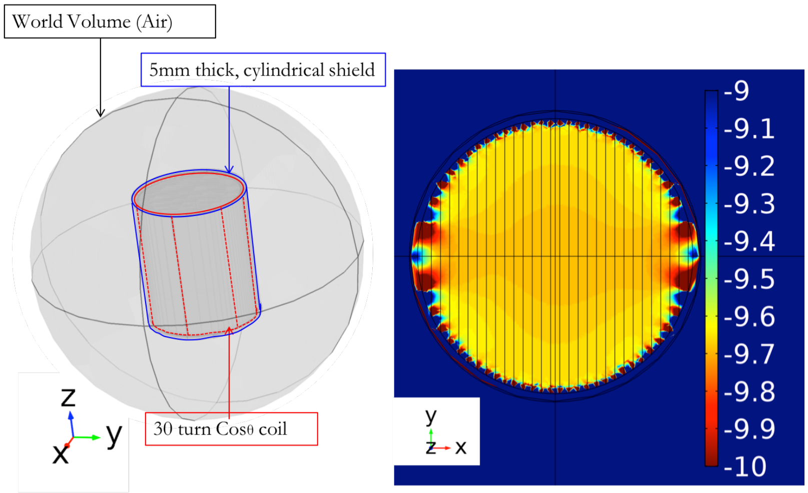

Figure 5.21: COMSOL Model

accuracy. Based on experimental geometry constraints, the new sensor array will be a cylindrical structure of radius and length of 24.5" and 48", respectively. This geometry was chosen based on the engineering design and constraints of the apparatus. As shown in Fig.4.3, the central detector region[5] sets the location and size for the magnetic field monitor. The array will consist of 5 planes at $z = \pm 24"$, $z = \pm 12"$ and $z = 0"$ and use 39 cryogenic single axis fluxgate magnetometer sensors (Bartington Mag F). The geometry for this prototype comes from studies done using a COMSOL model of a 30-turn, cylindrical $\cos\theta$ coil within a 5mm-thick cylindrical shield for which the field profile is shown in Fig.5.21.

The number of sensors was determined in order to optimize the reconstruction of the field profile and increase the sensitivity to shifts in the gradients as will be shown in the following sections. Because the main holding field will be oriented along the x direction, we want to maximize our sensitivity to field profile reconstruction for this component. From Fig.5.22, it is clear that in order to reconstruct the field in the region of interest, we need to be able to access up to the $\ell = 5$ basis functions in the scalar potential (Tables B1, B2, B3). For gradient reconstruction, it is important to have knowledge of $\frac{dB_x}{dy}$, where y is the direction along the length of the measurement cells, as this has a large effect on T_2, the transverse spin relaxation[57]. These factors are used to optimize the locations of the sensors for each sensor orientation.

5.4.2 Field Profile and Gradient Reconstruction

Our first studies consisted of our ability to reconstruct the field profile within the region of interest, i.e., within the region of the measurement cells. The boundary values were extracted from the COMSOL model at the optimal locations and used

---

[5] The Central Detector System (CDS) is the region that consists of the measurement cells, electrodes used to apply the electric field, SQUID magnetometers and scintillation light collections system.

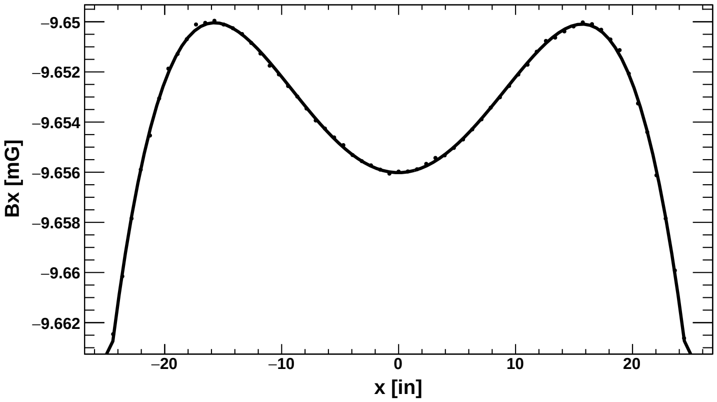

Figure 5.22: Field profile of B_x interior to the sensor array.

to determine the accuracy with which we are able to reconstruct the field. Fig.5.23 shows the results of the reconstruction. Within the region of the measurement cells[6], the RMS errors between the reconstructed and model field values for B_x along the x, y and z axes are 0.05%, 0.05%, and 0.07%, respectively. These values are quite good and demonstrate the robustness of this method.

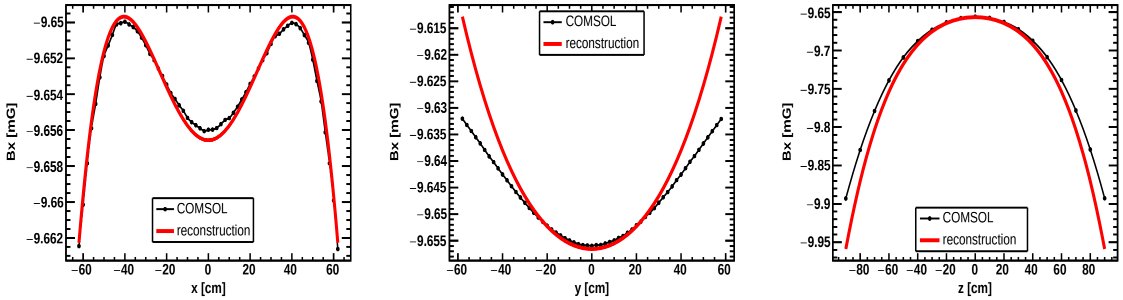

Figure 5.23: Reconstruction of B_x along x,y and z axes from COMSOL model boundary values.

Because it is important for the experiment to be able to control the magnetic field gradients, we need to have accurate knowledge of the linear gradient within the cells. To test the capability of this method to reconstruct linear gradients, we simulate a linear gradient of the form

$$\vec{B}_1 = a(x+y+z)\hat{\mathbf{x}} + a(x+y-2z)\hat{\mathbf{y}} + 2a(x-y-z)\hat{\mathbf{z}} \tag{5.25}$$

where a is a varying parameter. This gradient is then added to the simulated holding field B_0. By changing the parameter a, we can determine the limitation of our reconstruction of the linear gradient. Note that $\vec{B}_1$ satisfies Maxwell's equations.

---

[6] In the experiment, the measurement cells are made of poly(methyl methacrylate) and consist of two rectangular cells that are 10.16cm ×12.70cm×42cm in outer dimension with the walls being 1.2 cm thick.

In order to determine the accuracy of our reconstruction, we extract the linear gradient parameter for each component of the magnetic field along the direction of the field B_0, represented by P_3 in the equations below.

$$\begin{aligned} B_x &= -P_1 - x \cdot P_3 + ... \\ B_y &= -P_2 - y \cdot P_3 + ... \\ B_z &= -P_0 + 2z \cdot P_3 + ... \end{aligned} \tag{5.26}$$

The gradient study was done for the values of parameter a shown in Table 5.3.

Table 5.3: Result of reconstruction of the linear gradient parameter.

Linear Gradient Parameter Input (mG cm^{-1})	Linear Gradient Parameter Reconstruction (mG cm^{-1})
-1.000×10^{-2}	-1.000×10^{-2}
-1.005×10^{-3}	-1.008×10^{-3}
-1.012×10^{-4}	-1.194×10^{-4}

We can see that this method is reliable for reconstructing gradients down to $10^{-3}\ \frac{\text{mG}}{\text{cm}}$. However, gradients at or below $10^{-4}\ \frac{\text{mG}}{\text{cm}}$ are no longer accessible via this method. Because $\frac{dB_0}{dy}$ contributes significantly to T_2, we wanted to test our ability to reconstruct the corresponding linear gradient parameter as well.

Table 5.4: Result of reconstruction of the linear gradient parameter.

Linear Gradient Parameter Input (mG cm^-1)	Linear Gradient Parameter Reconstruction (mG cm^-1)
1.668×10^{-3}	1.663×10^{-3}
1.668×10^{-4}	1.667×10^{-4}
1.668×10^{-5}	1.380×10^{-5}

Thus we can see that we are able to reliably reconstruct the linear gradient parameter for $\frac{dB_0}{dy}$ down to a gradient of $10^{-4}\ \frac{\text{mG}}{\text{cm}}$.

5.4.3 Simulation Studies of Systematics

All of the results presented previously were based on ideal boundary value measurements extracted from the COMSOL model. In fact, the previous studies did not take into account errors that can arise from several factors such as the misalignment of the sensors with respect to the B_0 coil or the inherent offsets of the sensors. We performed several simulation studies to determine how these factors would affect the accuracy and reliability of our reconstructions.

5.4.3.1 Effect of Probe Offsets on the Reconstruction of Magnetic Field

In order to model the effect of the sensor offsets on the reconstruction of the linear gradients, we model the following boundary values to be used for the reconstruction

$$B^i_{bv} = B^i_0 + B^i_{grad} - B^i_{off} \tag{5.27}$$

where B^i_{bv} represents the "true" measurement one would read and

$$B^i_{off} = \frac{b}{20}(1 - 2 \cdot b) \tag{5.28}$$

where b is a parameter which we allow to vary randomly between each iteration of the reconstruction. By allowing the b parameter to vary, we are able to see the effect that drifting offsets have on the reconstruction of the linear gradient parameter. For our studies we allowed b to vary from -0.05 mG to 0.05 mG based on physical measurements of the offsets of several Bartington Mag F fluxgate magnetometer sensors. The results are shown in Fig.5.24.

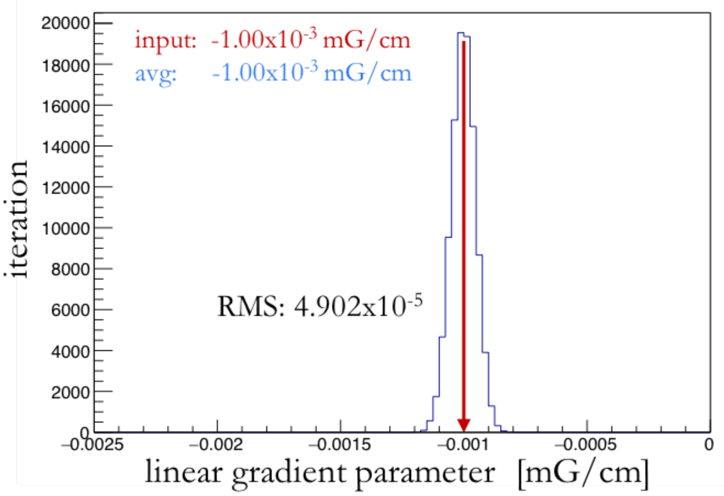

Figure 5.24: Reconstruction of linear gradient parameter with drifting offset.

The effect of the drifting offset of the sensors has some effect ($\sim 2.2\%$ error) on our ability to accurately reconstruct the linear gradient parameter. Because of this, it is imperative that we understand the inherent offsets, as well as the temporal stability of the offsets, of the Bartington Mag F sensors. These studies are currently under way.

5.4.3.2 Effect of Probe Misalignment on the Reconstruction of Magnetic Field

Another possible source of error in the reconstruction can arise from the misalignment of the sensor with respect to a fixed coordinate system. To simulate this effect, the boundary values extracted from the COMSOL model were rotated by some arbitrary angle and used in the reconstruction of the linear gradient parameter. These boundary values are of the form

$$B^i_{\text{bv}} = B^i_{\text{COMSOLrot}} + B^i_{\text{grad}} \tag{5.29}$$

where B^i_{off} is of the same form as Eq. 5.28 and $B_{\text{COMOSLrot}}$ is given by

$$\begin{aligned} B^x_{\text{rot}} &= B^x_{\text{bv}} \cos c + B^y_{\text{bv}} \sin c \\ B^y_{\text{rot}} &= -B^x_{\text{bv}} \sin c + B^y_{\text{bv}} \cos c \end{aligned} \tag{5.30}$$

where c is the rotation parameter. In our model we let c vary from 0° to 1°. The result of this study is shown in Fig.5.25. The results of this study demonstrate the importance of careful alignment not only of the sensors with respect to each other but also of the array with respect to the direction of the B_0 field. This is taken into consideration when designing the sensor array and mounts which will be described in the following section.

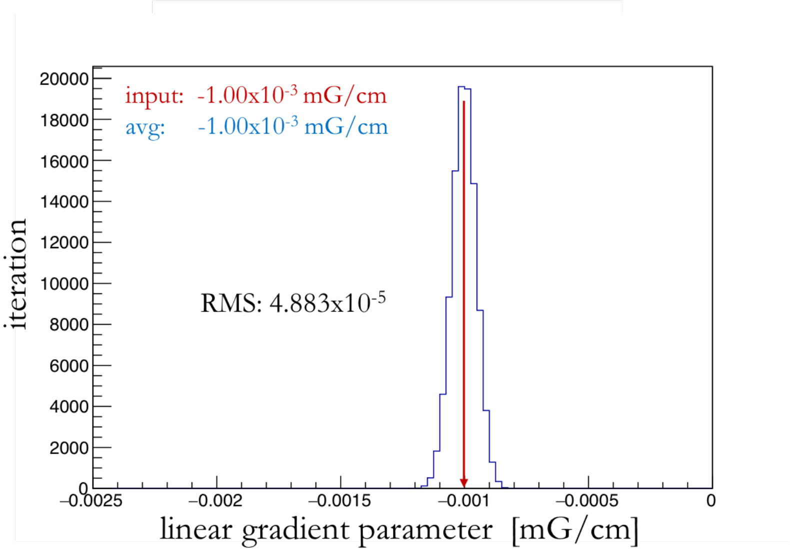

Figure 5.25: Reconstruction of linear gradient parameter with random rotation of the boundary values.

5.4.4 Studies using third scale B0 coil

The reconstruction of the 39 probe array was tested experimentally using the 1/3 scale B_0 coil. The coil was mounted on top of an 80/20 aluminum frame and a set of Helmholtz field cancellation coils mounted around it to cancel as much of the background field as possible. A set of anti-Helmholtz coils was also installed in order to apply gradients for reconstruction. The boundary values were measured using one Bartingon triple axis probe that was moved to the location of the boundary values. The reconsturctions were compared to the field scans along each axis. The experimental setup is shown in Fig.5.26.

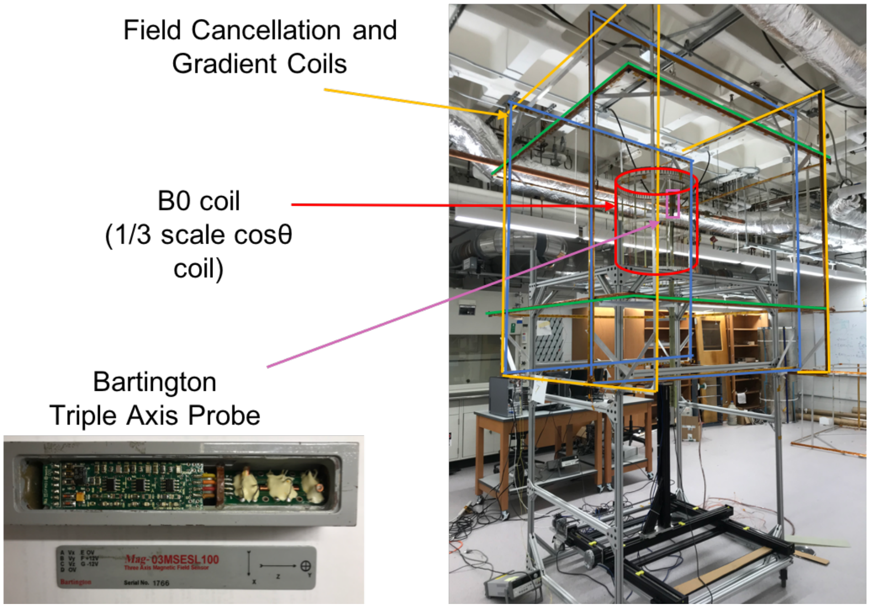

Figure 5.26: Experimental setup used to test the 39 sensor array. The third scale $\cos\theta$ coil was used to produce the magnetic field. A set of Helmholtz and anti-Helmholtz coils were set up around the $\cos\theta$ coil to cancel out the background magnetic fields as well as apply linear gradients for reconstructions. The boundary values were measured using a Bartington triple axis probe (Mag-03MSESL100) that was moved to the locations of the boundary values using a three axis magnetic field mapper.

The results of this study are shown in Fig.5.27 and the linear gradients for B_x averaged along the x, y, and z axes are shown in Table 5.5.

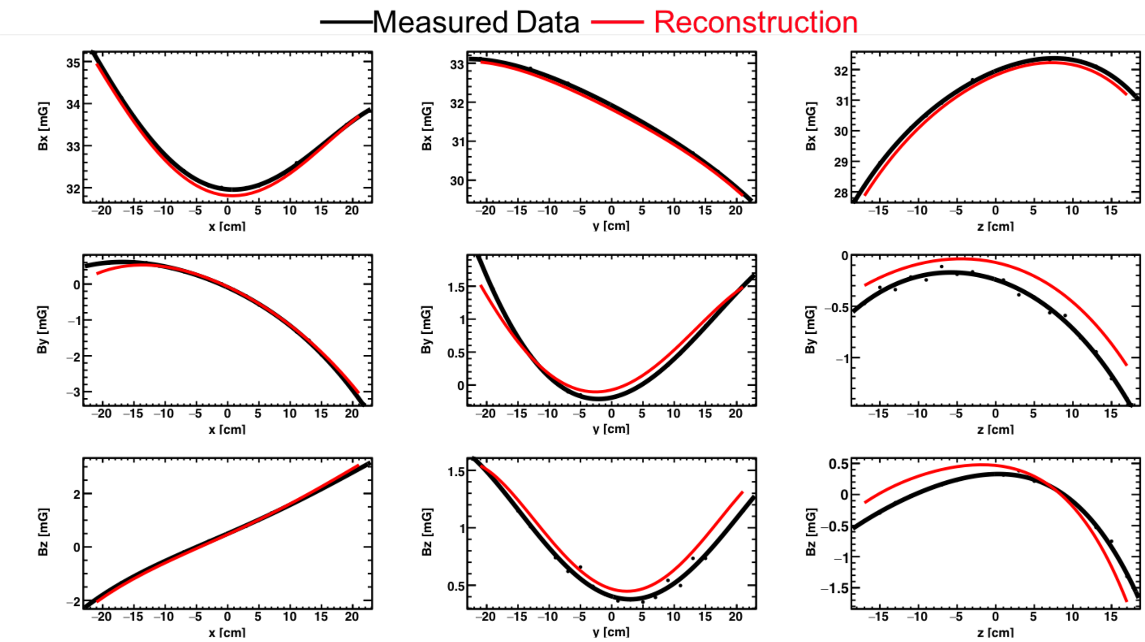

Figure 5.27: Reconstruction of the third scale $\cos\theta$ coil. The black curves represent the measured data and the red curves are the reconstruction.

Table 5.5: Reconstruction of the average linear gradient of the B_x component along the x, y and z axes.

Component	Measured (mG/cm)	Reconstructed (mG/cm)
$\langle \mathbf{dB_x/dx} \rangle$	-0.035	-0.032
$\langle \mathbf{dB_y/dx} \rangle$	-0.081	-0.081
$\langle \mathbf{dB_z/dx} \rangle$	0.087	0.089

We have demonstrated that we are able to reconstruct linear gradients to within $\sim$ 3.5% within the region of the array. In order to improve these results would require a shield to be constructed[7] around the B_0 coil to minimize the background fields and shield out fluctuations in the background that result from the construction equipment that is on during the data taking time.

An important goal of this field monitor system is the ability to monitor changes in the linear gradients. To test this capability, the current in the anti-Helmholtz gradient coils was changed in order to shift the linear gradient by a small amount, $\Delta(dB_x/dx) \sim 0.008$mG/cm. The results for the B_x component along the x-axis is shown in Fig.5.28 and Table 5.6.

---

[7] The experimental setup can be placed inside of MuMetal shielding.

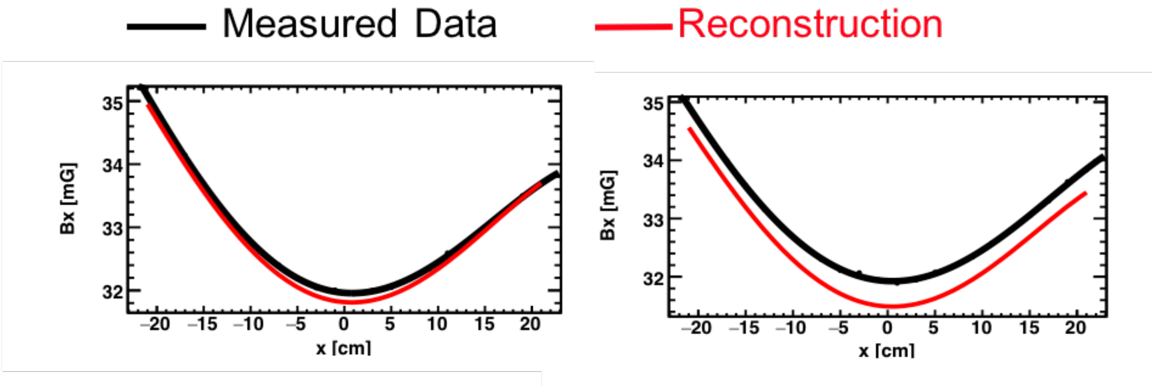

Figure 5.28: Comparison of the reconstruction of the B_x component along the x-axis after a small change in the linear gradient. The black curves represent the measured data and the red curves are the reconstruction.

Table 5.6: Reconstruction of the average linear gradient of the B_x component along the x axis for two different gradient settings.

Component	**Measured (mG/cm)**	**Reconstructed (mG/cm)**
$\langle \mathbf{dB_x/dx} \rangle$	-0.035	-0.032
$\langle \mathbf{dB_x/dx} \rangle$	-0.027	-0.028

These results show that we are able to track small gradient changes.

5.4.5 Mechanical Design of Sensor Array

In order to meet the geometrical requirements of the full experimental setup, the 39 sensor array geometry is a cylindrical structure 48" in length and 23.5" in radius. The array is constructed of 5 planes at $z = \pm 20"$, $z = \pm 12"$, and $z = 0$ (Fig.5.29a).

The spaceframe is a structure consisting of hoops, story sticks[8] and stiffening gussets, all of which are fabricated using sanded glass-fiber reinforced plastic (G-10)(Fig.5.31). This material is utilized because it is stable and stiff and has well known thermal properties.

Because the hoops are a little larger than readily available G-10 sheets, they are broken up into segments. If care is taken in how the segments are cut from the base material, the fiber warp and weft will be reasonably consistent traversing tangentially around each of the hoops. There is a difference in the magnitude of the thermal contraction in the warp and weft of the composite, and this segmentation helps prevent

---

[8] Oftentimes used in woodworking, a story stick is a slender piece of material that holds a series of markings designating the exact locations and profiles of critical elements of the piece being machined. Story sticks are highly useful to minimize measuring errors.

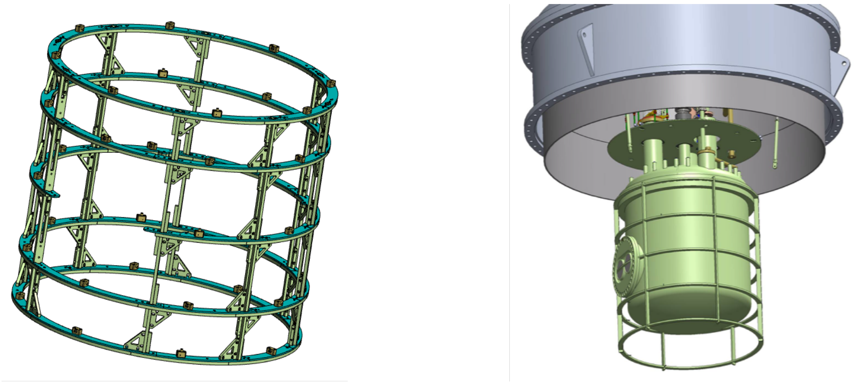

(a) Sensor array space-frame.

(b) Sensor array frame installed around the CDS.

Figure 5.29: Probe array space frame.

distortions of the space frame while cooling. The hoops are made from two layers (Fig.5.30a), with provisions to accommodate PEEK nuts and bolts, since the G-10 material does not generally yield good quality fastener threads. Each of the hoop segments is aligned with adjacent segments using a pair of custom spring pins, controlling relative positioning and rotation. The intent of this construction is to allow bolt-only assembly of the segments into rings (Fig.5.30b). As a fallback, they may be glued using DP-190 epoxy to ensure long-term repeatability.

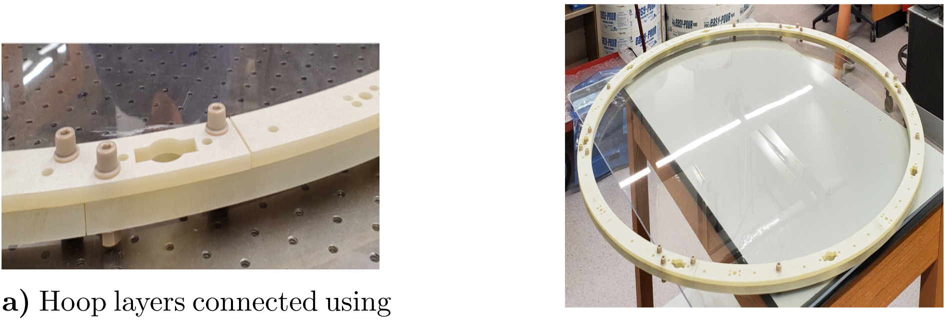

(a) Hoop layers connected using PEEK nuts, bolts and washers.

(b) Hoop segments assembled into a ring.

Figure 5.30: Hoop

Several of the segments are intended to be dismountable to account for assembly of the structure into the Central Detector Module (Fig.5.29b) and also to accommodate different sensor configurations during testing.

The story sticks include notches that dictate vertical positioning of the hoops during assembly. The gussets are used to join the hoops to the story sticks and provide additional stiffness to the overall assembly. There will be 5 hoops, each fabricated from 16 segments (except at Z=0, where there are 14 segments. There are 8 story sticks and 52 gussets, and 28 gusset backing blocks. These components will be bolted together using PEEK hardware.

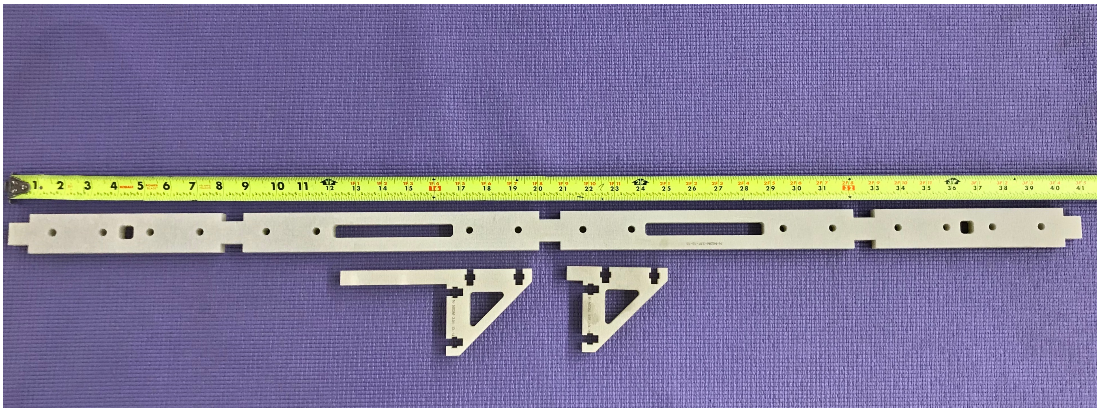

Figure 5.31: Story stick and gussets.

The Bartington probes are not perfectly consistent in diameter or length, yet it is necessary to locate their geometric center in space with some precision. To accomplish this, the sensors will be individually fit into Torlon bushings that will in turn fit into Torlon blocks as shown in Fig.5.32. The blocks are mounted to the sensor support spaceframe via PEEK nuts and bolts (④ and ⑤ in Fig.5.32) as shown in Fig.5.33b.

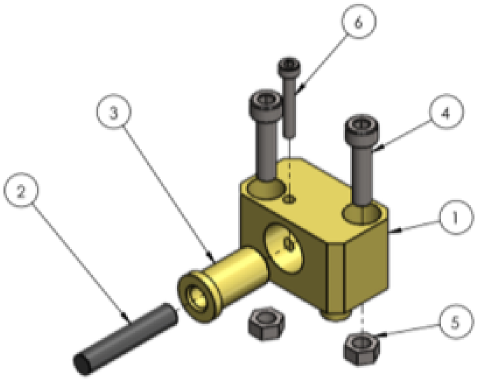

Figure 5.32: Block and bushing assembly. ① Torlon block, ② Bartington probe ③ Torlon bushing, ④ PEEK bolt,⑤ PEEK nut, ⑥ PEEK set screw

All of the G-10 components of the spaceframe were cut from the stock sheet using waterjet. This concept has been proven effective and relatively inexpensive and has yielded appropriate manufacturing tolerances. The sensor bushing and mount blocks were fabricated using Torlon 4203, since it performs well in a cryogenic environment,

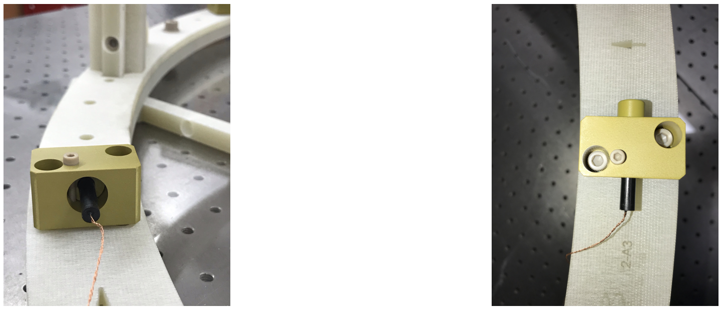

(a) Probe, Bushing and Block **(b)** Probe, Bushing and Block

Figure 5.33: Probe, Bushing and Block

is readily available and machinable, and matches the thermal movement of the G-10 in the warp direction reasonably well. For this reason, this Torlon grade is also used for the adjustable pin components that will attach this assembly to the central liquid helium volume.

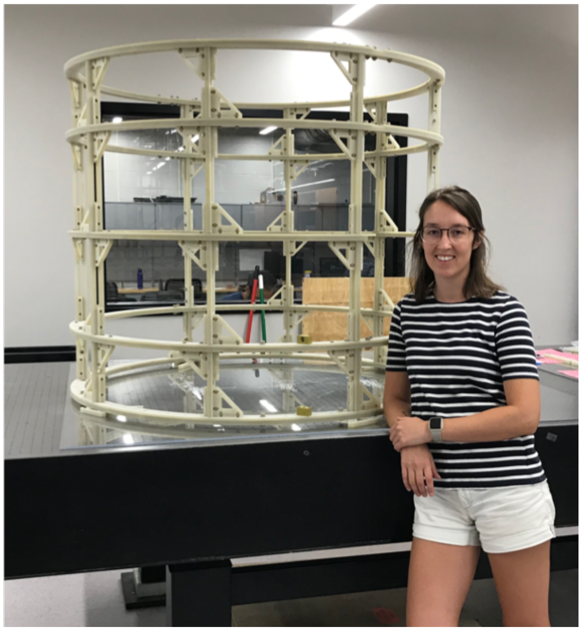

Figure 5.34: Fully assembled magnetic field monitor spaceframe with graduate student for scale.

5.4.6 Readout Electronics for Sensor Array

In lieu of a manual switching box, we have designed a fully automated switching system for the 39 sensor probe array (Fig.5.37). This will allow the user to take boundary value data much more efficiently than with the previous mechanical switching system.

Each sensor will be controlled by four Reed relays corresponding to the excitation and feedback wires. We are using Reed relays that have an internal mu-metal magnetic screen in order to prevent interference and desensitizing of adjacent relays. The boundary value measurements will be performed sequentially, thus only four relays will be powered at a time.

The sensor wires will pass from the vacuum chamber to the switching box via a vacuum feedthrough (Figs.5.35, 5.36) where they will be connected by four sets of twisted pair ribbon cables (10 sensors per set, Amphenol cables) to a circuit board. The connection to the circuit board will be via a flat cable type rectangular socket connector for ease of making the connection to the circuit board as well as provide strain relief to the ribbon cables.

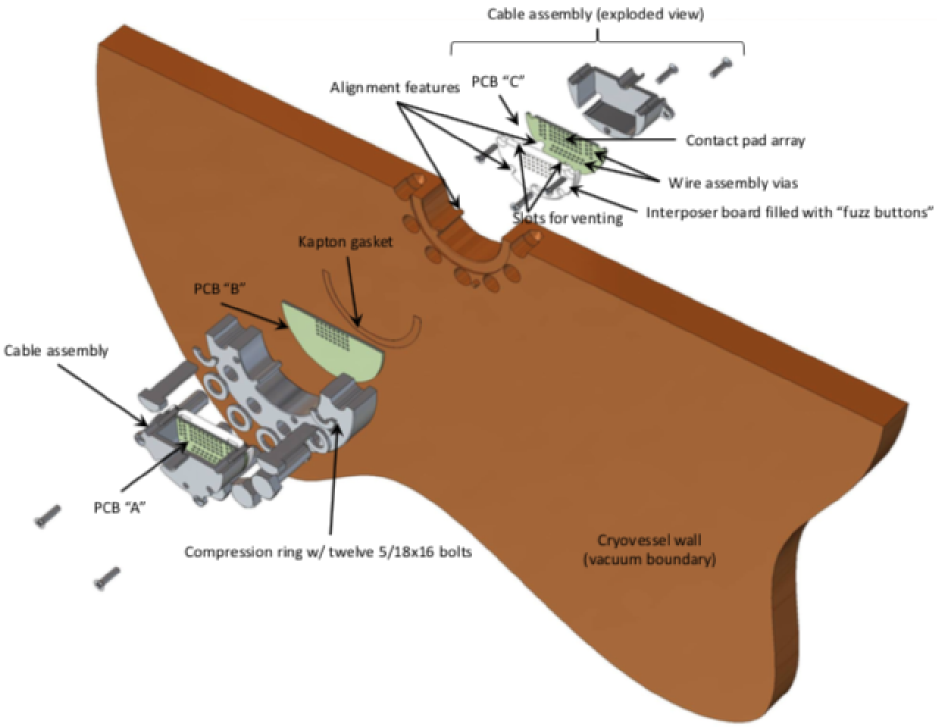

Figure 5.35: Non-magnetic cryogenic multi-conductor vacuum feedthrough.[58]

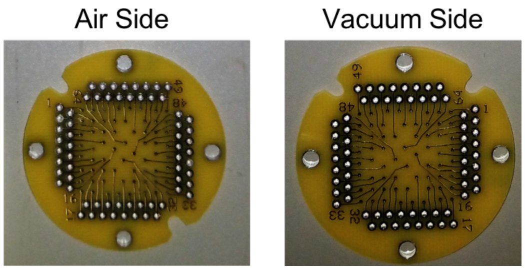

Figure 5.36: Non-magnetic feedthrough PC board. The left side panel shows the PCB "A" component and the right side panel shows the PCB "C" component from Fig.5.35.

The circuit will be controlled by a microcontroller. The analog signal, corresponding to a measurement made by the sensor, from the Mag-01H magnetometer will be fed into a Sigma-Delta ADC and read into an Excel or text file.

The switching unit will be enclosed in an Al box of dimensions $\sim 8.23" \times 7.0" \times 2.4"$. The Mag-01H unit ($6.9" \times 6.1" \times 2.7"$) will sit on top of the switching box.

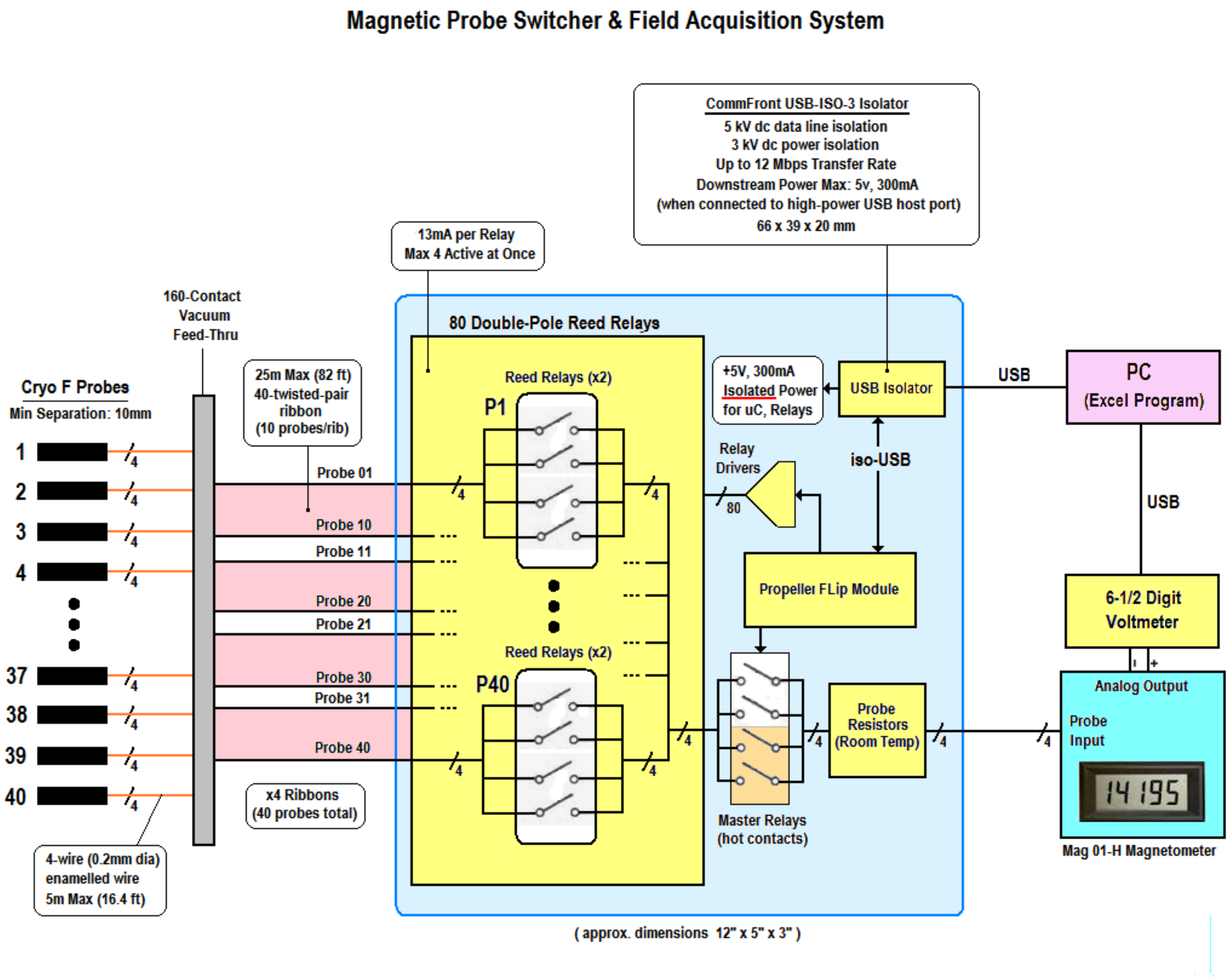

Figure 5.37: Schematic of the Switching Box

5.4.6.1 Studies of the Switching Box Prototype

A two fluxgate prototype of the switching box was built to perform several tests before building the final switching electronics.

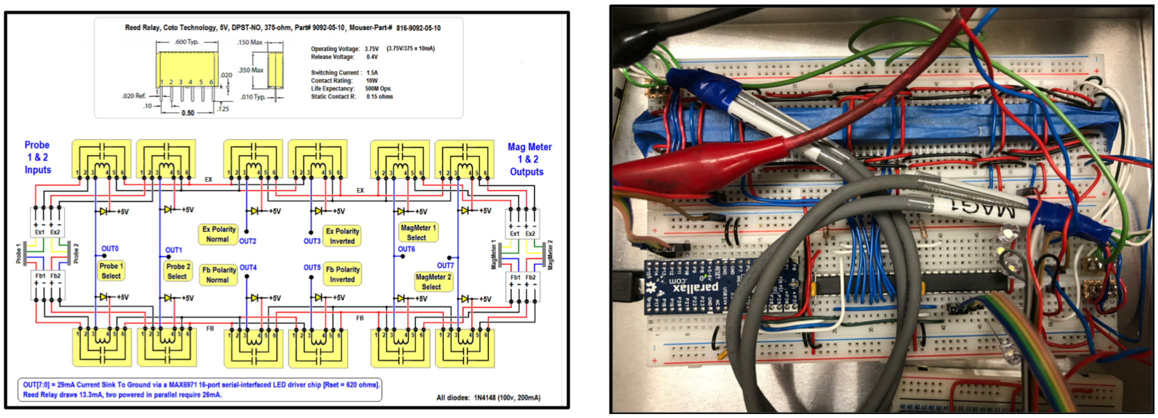

Figure 5.38: Switching Box Prototype.

One such test was designed to measure the response time when switching between two sensors. In the experiment, 24 of the sensors (B_x) will be measuring a high field ($\sim 3\mu T$) and 19 (B_y and B_z) will be measuring a low field ($\sim$ 100nT) so it is important that the switching allows for each sensor reading to stabilize before recording the boundary value. Once the field reading is stabilized, a measurement is acquired within 1 ms.

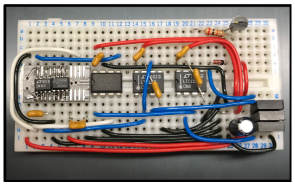

Figure 5.39: Stable current source.

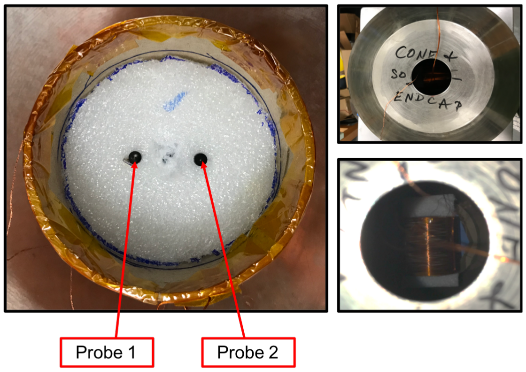

Figure 5.40: Experimental setup testing switching response time for sensors measuring nearly the same field.

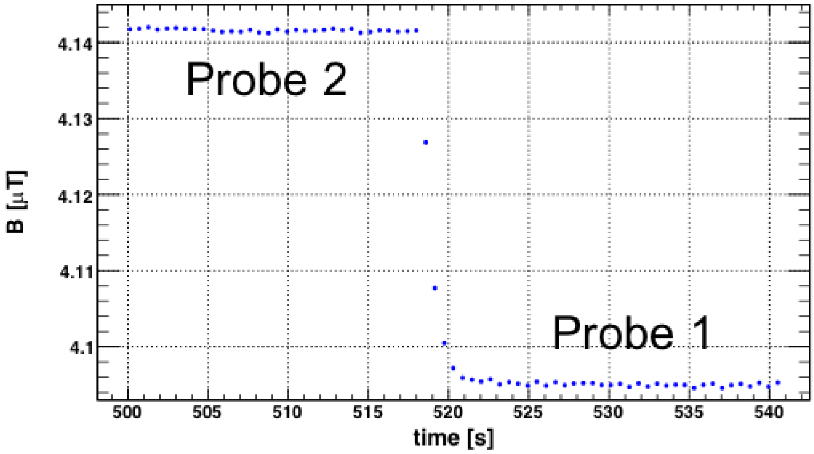

Figure 5.41: Response time between two sensors. It takes approximately 3 seconds for the reading to stabilize.

Based on the results (Fig.5.41) of this test, it will take ∼ 3 s for the readings to stabilize to within 0.5 nT. This would allow for the full set of boundary value measurements to be made within 2 minutes.

5.4.6.2 Phosphor Bronze Wire Analysis

The probe array will be mounted to the central detector system (CDS) and be kept at a temperature of ∼ 4 K (Fig.5.42). It is important to consider the heat load from the probe wires to the CDS 4 K bath. For 156 conductors (4 conductors per sensor, 0.2mm Cu) this contributes ∼ 1 W.

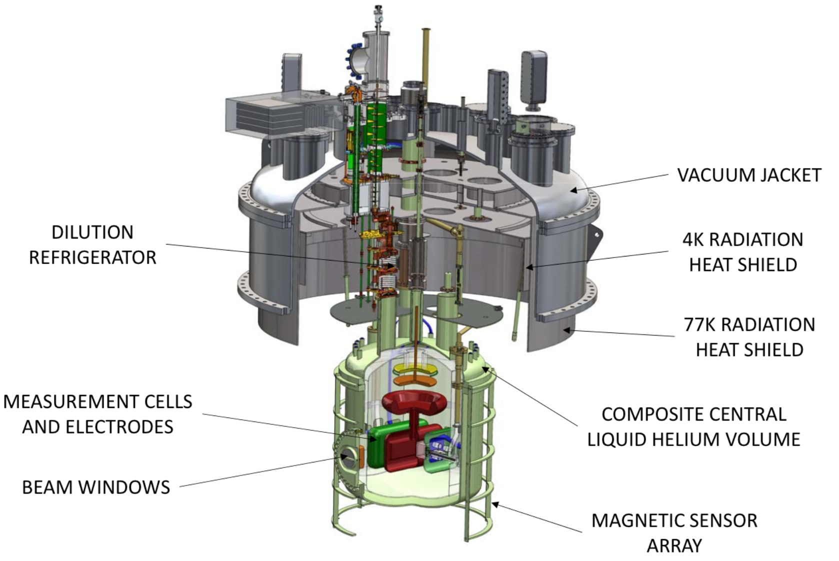

Figure 5.42: Overview of the Central Detector System (CDS).[45]

In order to reduce the heat load to the system, a 0.8m section of the enameled Cu wire within the CDS region can be replaced with 32 AWG phosphor bronze wire[9] as illustrated in Fig.5.43. This substitution would greatly reduce the heat load but at the expense of additional resistivity[10].

(a) Wire layout diagram with 0.2mm diameter enamel Cu wire only.

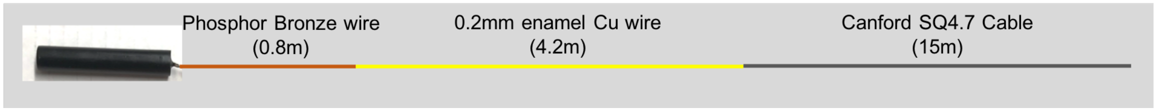

(b) Wire layout diagram with 0.8m phosphor bronze wire substitution.

Figure 5.43: Wire layout with and without the phosphor bronze wire.

---

[9] The thermal conductivity of copper is 300 W/(m·K) while that of phosphor bronze is 1.6 W/(m·K) at a temperature of 4 K [59].

[10] The resistivity of Cu is 1.7 $\mu\Omega$·cm while that of phosphor bronze is 11 $\mu\Omega$·cm at 293 K [59].

Table 5.7: Specifications for phosphor bronze wire.[59]

AWG	Resistance (Ω/m)			Diameter (mm)
	4.2 K	77 K	305 K	
32	3.34	3.45	4.02	0.203
36	8.56	8.83	10.3	0.127

The possible effect of the added resistance from the use of phosphor bronze wire on either the primary or pick up coils can have an effect if the resistance added is too high and prevent sufficient current going through the coils thus preventing the cores reaching saturation, or the resistance added is too high so that the electronics cannot drive the necessary current into the pick up coil. Because of this, it is necessary to conduct several experiments to determine the effect that the added resistance will have on the signal. Fig.5.44 shows the circuit used to add extra resistance to the probe wires. The circuit uses a set of Reed relays to introduce additional resistance to the system. The circuit allows us to switch between a loaded (extra resistance added) and unloaded (no extra resistance added) system.

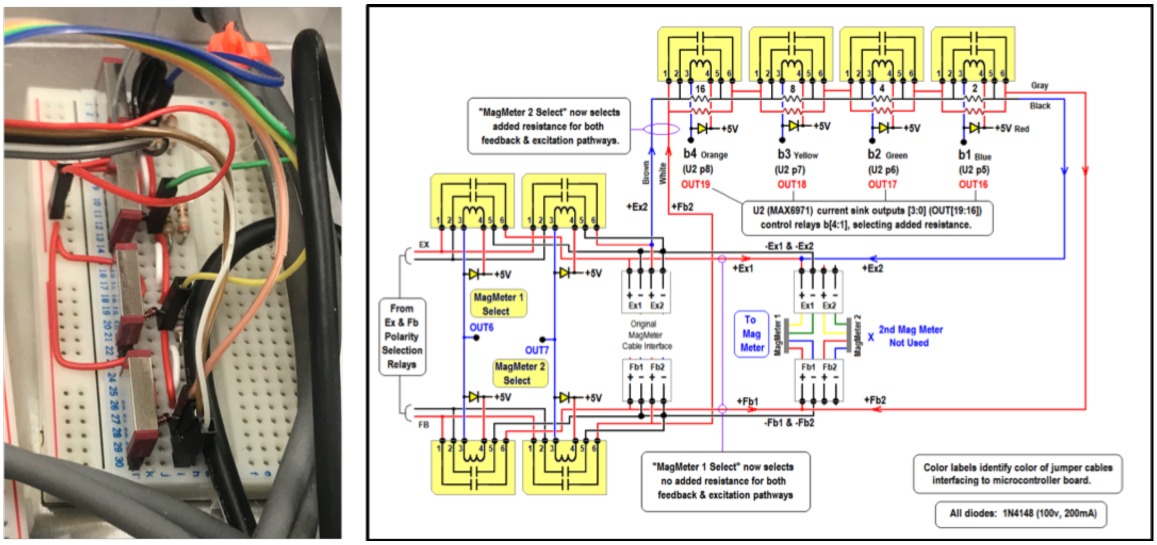
"MagMeter 2 Select" now selects added resistance for both feedback & excitation pathways.

U2 (MAX6971) current sink outputs [3:0] (OUT[19:16]) control relays b[4:1], selecting added resistance.

"MagMeter 1 Select" now selects no added resistance for both feedback & excitation pathways

Color labels identify color of jumper cables interfacing to microcontroller board.

All diodes: 1N4148 (100v, 200mA)

Figure 5.44: Circuit to control added resistance load to the excitation and feedback probe wiring. The circuit adds resistance from 0 Ω to 30 Ω in steps of 2 Ω.

The first test performed was to load the excitation probe wires only and then the feedback probe wires only with an extra resistance of 20 Ω to determine where this will have the largest effect. Figure 5.45 shows that the added resistance will have the most effect on the excitation coil as initially predicted.

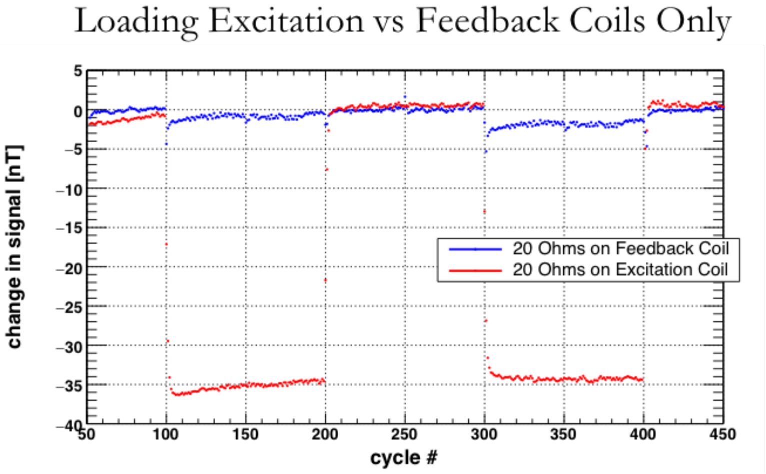

Figure 5.45: The effect of adding extra 20 Ω to the feedback (blue) or excitation (red) probe wires only.

The added resistance test was then repeated for two different probes adding extra resistance to the excitation probe wires in steps of 10 Ω. The results shown in Fig.5.46 indicate that there is a large offset in the signal with additional resistance. The effect between two separate probes is of approximately the same size. This indicates that, having precise knowledge of the extra added resistance, the signal offset can be calibrated for all sensors being used.

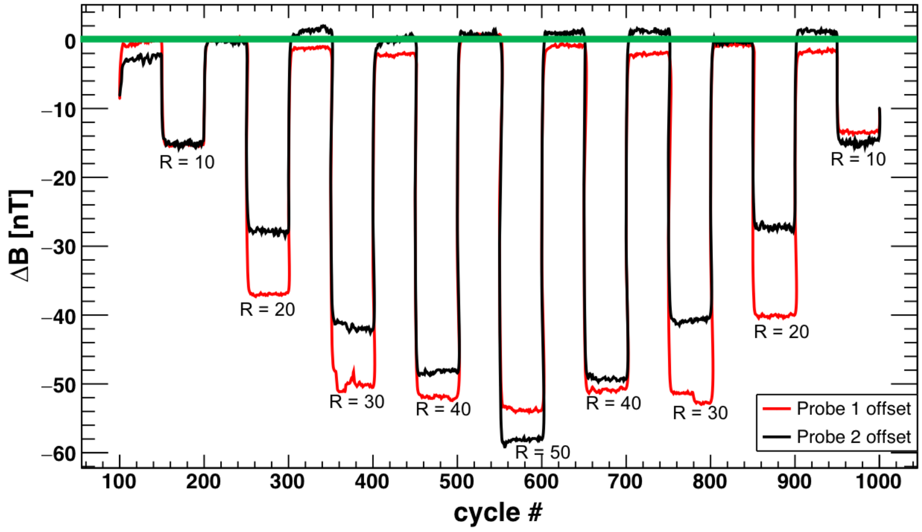

Figure 5.46: The effect of adding extra resistance to the wires of two different probes for five different values of resistance (in units of Ω). The plot shows the signal offset (ΔB) from the true value (defined by the field measured by a probe without extra resistance added) of the magnetic field.

Because the probe array will be maintained at ~ 4 K during the experimental run, this test was repeated for different extra added resistance values in liquid nitrogen and at room temperature. These results are shown in Fig.5.47.

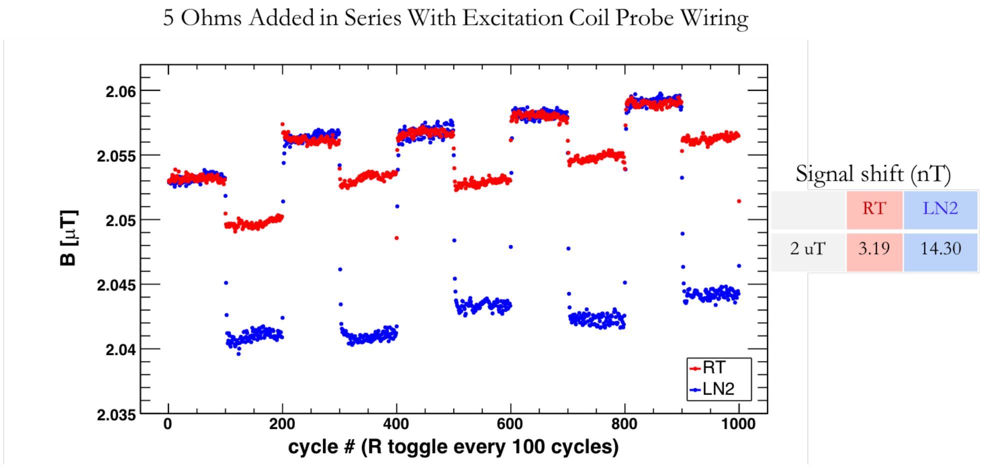

Figure 5.47: The effect of adding extra resistance to the wires of a single probe at two different temperatures.

The effect of the added resistance is much more pronounced at cryogenic temperature than at room temperature. The source of this effect is still under investigation and further testing is ongoing. It is also interesting to note that a similar effect is observed if the extra resistance test is done for a single probe at two different applied magnetic fields (Table 5.8).

Table 5.8: Signal offset for a single probe measured in several different applied fields and at two different temperatures when 5 Ω of extra resistance is added to the probe wires.

Applied Field (μT)	**Signal Offset (nT)**	
	300 K	**77 K**
6.5	13.38	18.29
3.5	5.06	15.35
2	3.19	14.30
0.07	0.43	5.82

In an attempt to minimize the signal offset when extra resistance is added to the probe wire, the resistance tests discussed were repeated with a simultaneous increase in the amplitude of the excitation voltage provided to the probe. This was achieved by increasing the gain of the op-amp within the Mag-01H unit.

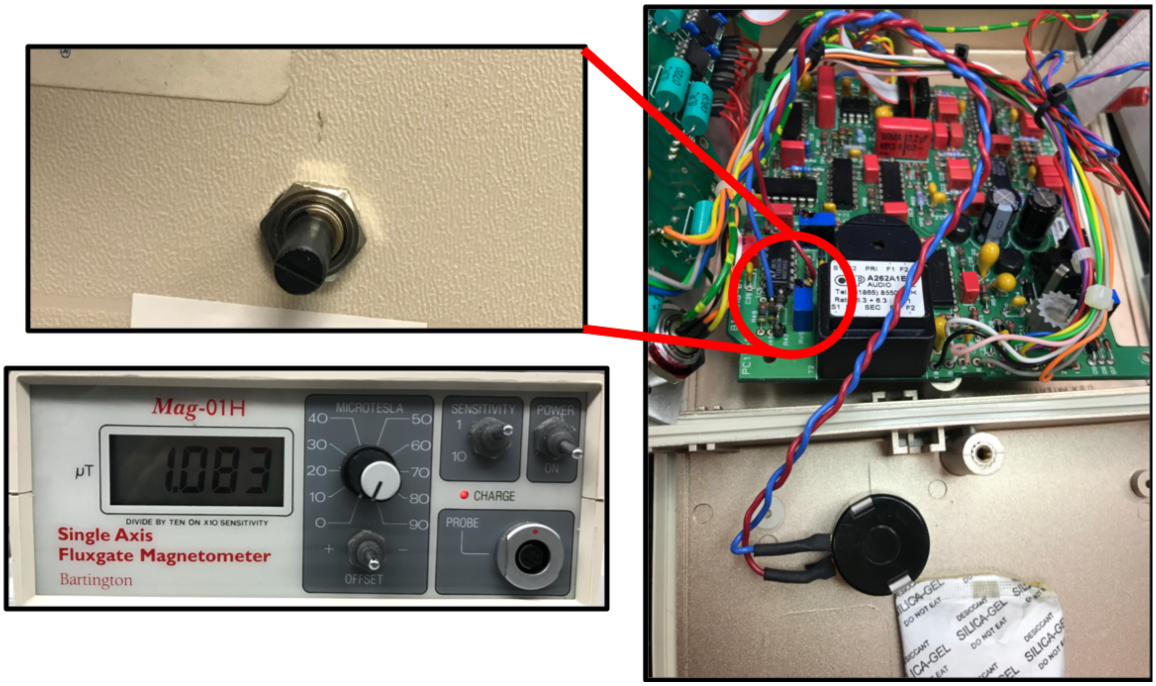

Figure 5.48: The excitation voltage can be increased(decreased) by adjusting the gain of the op-amp prior to the step down transformer. This can be done via a 10 turn dial that was wired external to the Mag-01H unit.

Table 5.9: Signal offset for a single probe measured in several different applied fields and in liquid nitrogen when 20 Ω of extra resistance is added to the probe wires. The signal offset is measured before and after the amplitude of the excitation voltage is increased by 75%.

Applied Field (μT)	**Signal Offset (nT)**	
	77 K before gain adjustment	**77 K** after gain adjustment
6	66	48
3	20	17
0.2	5	0.02

From Table 5.9, it is clear that increasing the gain of the excitation voltage decreases the signal offset from the extra resistance. In the tests done, the excitation voltage was increased by 75% for all trials. This gain adjustment can be automated and calibrated to adjust to different values based on the applied field and operational temperature.

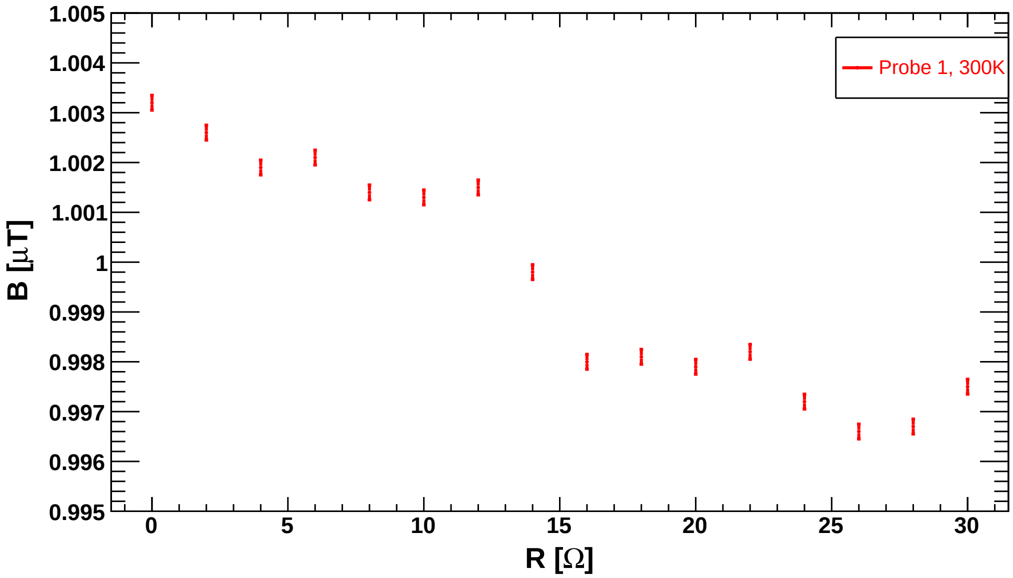

Figure 5.49: Signal response of a single probe as resistance is added to the probe wires in steps of 2Ω.

Based on the results shown in Fig.5.46 and Table 5.49 and Table 5.9, if the added resistance is kept below ∼ 5 Ω, the offset of the signal can be minimized. This can be achieved by using an appropriate gauge of phosphor bronze wire (Table 5.7). The signal offset can then be calibrated at different magnetic fields and at different operating temperatures and taken into account as part of the probe offsets described in Sec. 5.3.1.1.

CHAPTER 6

CONCLUSION

The search for the neutron EDM has captivated physicists for many decades. It is an enticing probe to the search for physics beyond the Standard Model that might explain the baryon asymmetry in the universe. Many extensions to the Standard Model predict the existence of a neutron EDM as shown in Fig.6.1 [60].

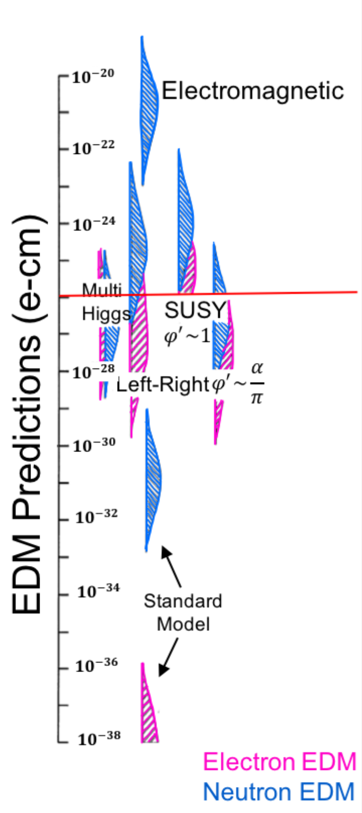

Figure 6.1: Various predictions for the neutron EDM from several SM extensions. The red line indicates the current world limit of 3.0×10^{-26}e cm.

In this way the nEDM serves as a test of such models and provides tight constraints on several of them.

The experimental search has led to the development of new and exciting experimental techniques. The need to increase the sensitivity of successive measurements requires the suppression of key systematic effects which many experiments have attempted to overcome. This thesis focused on the experiment that is currently under construction at the SNS at ORNL, and specifically on the magnetic field monitoring system that will be used.

The goal of the magnetic field array is to be able to monitor field gradients to the level of 10^{-5}cm^{-1} and we have shown with our third scale prototype that we are able to meet this goal. The full scale monitor has been constructed at the University of Kentucky and, upon the completion of the electronic control system, will be shipped to the California Institute of Technology for calibration and testing.

While this monitor was developed specifically for the use in the SNS nEDM experiment, we envision that it would be useful in many experiments where the knowledge of magnetic fields is important.

APPENDIX A

RABI SPIN FLIP

Suppose a spin-$\frac{1}{2}$ particle in a uniform magnetic field oriented along the z-axis, $B_0\hat{k}$. A rotating field is then applied in the xy-plane, perpendicular to The interaction of a magnetic moment in an external magnetic field is given by the Hamiltonian:

$$\mathcal{H} = -\vec{\mu} \cdot \vec{B}. \tag{A.1}$$

The magnetic field $\vec{B}$ is

$$\vec{B} = B_0\hat{k} + B_1\left(\cos(\omega_1 t)\hat{\imath} - \sin(\omega_1 t)\hat{\jmath}\right) \tag{A.2}$$

and $\vec{\mu} = \gamma\hbar\vec{S}$, where γ is the gyromagnetic ratio. The Hamiltonian can be written as:

$$\mathcal{H} = -\gamma\frac{\hbar}{2}\Big[B_0\sigma_z + B_1\big\{\sigma_x\cos(\omega_1 t) - \sigma_y\sin(\omega_1 t)\big\}\Big] \tag{A.3}$$

where σ_i are the Pauli spin matrices.

$$\mathcal{H} = -\gamma\frac{\hbar}{2}\begin{pmatrix} B_0 & B_1 e^{i\omega_1 t} \\ B_1 e^{-i\omega t} & -B_0 \end{pmatrix} \tag{A.4}$$

To see the evolution of the system in this field one needs to solve the time dependent Schrodinger equation:

$$i\hbar\frac{\partial}{\partial t}\left|\Psi(t)\right\rangle = \mathcal{H}\left|\Psi(t)\right\rangle \tag{A.5}$$

where

$$\left|\Psi(t)\right\rangle = \begin{pmatrix}\psi_+(t) \\ \psi_-(t)\end{pmatrix} \tag{A.6}$$

$$\Psi(t) = a(t)e^{-iE_+t/\hbar}\psi_+ + b(t)e^{-iE_-t/\hbar}\psi_- \tag{A.7}$$

and

$$\psi_+ = \begin{pmatrix}1 \\ 0\end{pmatrix} \quad \text{and} \quad \psi_- = \begin{pmatrix}0 \\ 1\end{pmatrix} \tag{A.8}$$

represent the spin-up $\psi_+ = \begin{pmatrix}1 \\ 0\end{pmatrix}$ state and $\psi_+ = \begin{pmatrix}0 \\ 1\end{pmatrix}$ the spin-down state.

The probability of finding the system in the spin up state is given by $|a(t)|^2$ and in the spin down state is given by $|b(t)|^2$.

One can determine $a(t)$ and $b(t)$ from:

$$i\hbar\frac{\partial}{\partial t}\begin{pmatrix} a(t)e^{-iE_+t/\hbar} \\ b(t)e^{-iE_-t/\hbar} \end{pmatrix} = -\gamma\frac{\hbar}{2}\begin{pmatrix} B_0 & B_1 e^{i\omega_1 t} \\ B_1 e^{-i\omega_1 t} & -B_0 \end{pmatrix}\begin{pmatrix} a(t)e^{-iE_+t/\hbar} \\ b(t)e^{-iE_-t/\hbar} \end{pmatrix} \tag{A.9}$$

where $E_+ = -\gamma B_0\hbar/2$ and $E_- = \gamma B_0\hbar/2$ as determined from the time independent part of the interaction.

From A.9, one obtains:

$$\begin{aligned} \dot{a}(t) &= i\frac{\gamma B_1}{2}e^{-i(\omega_1-\omega_0)t}b(t) \\ \dot{b}(t) &= -i\frac{\gamma B_1}{2}e^{i(\omega_1-\omega_0)t}a(t) \end{aligned} \tag{A.10}$$

$$\ddot{a}(t) = i\frac{\gamma B_1}{2}e^{-i(\omega_1-\omega_0)t}\dot{b}(t) + \frac{\gamma B_1}{2}(\omega_1-\omega_0)e^{-i(\omega_1-\omega_0)t}b(t) \tag{A.11}$$

Substituting $\dot{b}(t)$ and $b(t)$ from Eq.A.10 into Eq.A.11:

$$\begin{aligned} \ddot{a}(t) &= -\frac{\gamma^2 B_1^2}{4}a(t) + i(\omega_1-\omega_0)\dot{a}(t) \\ \ddot{a}(t) - i(\omega_1-\omega_0)\dot{a}(t) &+ \frac{\gamma^2 B_1^2}{4}a(t) = 0 \end{aligned} \tag{A.12}$$

This is a second order homogeneous differential equation and can be solved to give:

$$a(t) = e^{i(\omega_1-\omega_0)t/2}(c_1 e^{i\Omega t} + c_2 e^{-i\Omega t}) \tag{A.13}$$

where

$$\Omega = \frac{\sqrt{(\omega_1-\omega_0)^2 + \gamma^2 B_1^2}}{2} \tag{A.14}$$

and is known as the Rabi frequency.

The coefficients c_1 and c_2 can be determined from the initial conditions that the spins start out in the up state: $a(t=0) = 1$ and $b(t=0) = 0$.

The probability of a spin being found in the up state is given by $|a(t)|^2$ and in the down state is given by $|b(t)|^2$. Following the procedure above $b(t)$ can be calculated to be:

$$b(t) = \frac{i\gamma B_1}{\sqrt{(\omega_1-\omega_0)^2 + \gamma^2 B_1^2}}\sin\left(\frac{\sqrt{(\omega_1-\omega_0)^2 + \gamma^2 B_1^2}}{2}t\right) \tag{A.15}$$

and $|b(t)|^2$ is

$$|b(t)|^2 = \frac{\gamma^2 B_1^2}{(\omega_1-\omega_0)^2 + \gamma^2 B_1^2}\sin^2\left(\frac{\sqrt{(\omega_1-\omega_0)^2 + \gamma^2 B_1^2}}{2}t\right). \tag{A.16}$$

This is the Rabi equation and shows the probability of finding the spin in a down state after the application of some oscillating field. When $\omega_1 = \omega_0$, or the applied oscillating field is of the same frequency as the Larmor precession frequency, the probability of a spin flip will be maximum resulting in a resonance peak.

APPENDIX B

BASIS FUNCTIONS

Table B1 shows the basis functions used for the reconstruction of the B_x component.

Table B1: Basis functions for B_x used for reconstructions.

	$B_x(\vec{x})$
Coefficient	Basis Function
P_0	0
P_1	-1
P_2	0
P_3	$-x$
P_4	$-3z$
P_5	0
P_6	$6y$
P_7	$-3xz$
P_8	$\frac{3}{2}(3x^2+y^2-4z^2)$
P_9	$3xy$
P_{10}	$30yz$
P_{11}	$45(-x^2+y^2)$
P_{12}	$\frac{5}{2}xz(3(x^2+y^2)-4z^2)$
P_{13}	$-\frac{15}{8}(x^2(5x^2+6y^2)+y^4-12(3x^2+y^2)z^2+8z^4)$
P_{14}	$210(xz^3-x^3z)$
P_{15}	$\frac{105}{2}(-3y^2(6x^2+y^2)+24z^2(y^2-x^2)+5x^4)$
P_{16}	$3780x(x^2z-3y^2z)$
P_{17}	$4725(x^2(-x^2+6y^2)-y^4)$

Table B2 shows the basis functions used for the reconstruction of the B_y component.

Table B2: Basis functions for B_y used for reconstructions

Coefficient	$B_y(\vec{x})$ Basis Function
P_0	0
P_1	0
P_2	-1
P_3	$-y$
P_4	0
P_5	$-3z$
P_6	$6x$
P_7	$-3yz$
P_8	$3xy$
P_9	$\frac{3}{2}(x^2 + 3y^2 - 4z^2)$
P_{10}	$30xz$
P_{11}	$90xy$
P_{12}	$\frac{5}{2}yz(3(x^2 + y^2) - 4z^2)$
P_{13}	$\frac{15}{2}xy(x^2 + y^2 - 6z^2)$
P_{14}	$210yz(y^2 - z^2)$
P_{15}	$210xy(12z^2 - x^2 - 3y^2)$
P_{16}	$3780yz(y^2 - 3x^2)$
P_{17}	$18900xy(x^2 - y^2)$

Table B3 shows the basis functions used for the reconstruction of the B_z component.

Table B3: Basis functions for B_z used for reconstructions

	$B_z(\vec{x})$
Coefficient	Basis Function
P_0	1
P_1	0
P_2	0
P_3	$2z$
P_4	$-3x$
P_5	$-3y$
P_6	0
P_7	$-\frac{3}{2}(x^2+y^2-2z^2)$
P_8	$-12xz$
P_9	$-12yz$
P_{10}	$30xy$
P_{11}	0
P_{12}	$5(\frac{3}{8}(x^2+y^2)^2-z^2(3(x^2+y^2)-z^4))$
P_{13}	$15xz(3(x^2+y^2)-4z)$
P_{14}	$\frac{105}{2}(y^4-x^4+6z^2(x^2-y^2))$
P_{15}	$840xz(3y^2-x^2)$
P_{16}	$945(x^4-6x^2y^2+y^4)$
P_{17}	0

APPENDIX C

SENSOR LOCATIONS

Table C1 shows the locations and orientations for the 39 Bartington Mag F probes on the array structure.

Table C1: Sensor Locations

Location Number	ϕ	z(in)
1 (B_x)	0	20
2 (B_x)	$\frac{\pi}{4}$	20
2 (B_y)	$\frac{\pi}{2}$	20
4 (B_x)	$\frac{3\pi}{4}$	20
5 (B_x)	π	20
6 (B_x)	$\frac{5\pi}{4}$	20
7 (B_y)	$\frac{3\pi}{2}$	20
8 (B_z)	$\frac{7\pi}{4}$	20
9 (B_y)	0	12
10 (B_x)	$\frac{\pi}{4}$	12
11 (B_x)	$\frac{\pi}{2}$	12
12 (B_z)	$\frac{3\pi}{4}$	12
13 (B_x)	π	12
14 (B_x)	$\frac{5\pi}{4}$	12
15 (B_y)	$\frac{3\pi}{2}$	12
16 (B_x)	$\frac{7\pi}{4}$	12
17 (B_x)	0	0
18 (B_x)	$\frac{\pi}{4}$	0
19 (B_x)	$\frac{\pi}{2}$	0
20 (B_y)	$\frac{3\pi}{4}$	0
21 (B_x)	pi	0
22 (B_x)	$\frac{5\pi}{2}$	0
23 (B_z)	$\frac{7\pi}{4}$	0
24 (B_x)	0	-12
25 (B_x)	$\frac{\pi}{4}$	-12
26 (B_y)	$\frac{\pi}{2}$	-12
27 (B_z)	$\frac{3\pi}{4}$	-12
28 (B_x)	π	-12
29 (B_x)	$\frac{5\pi}{4}$	-12
30 (B_x)	$\frac{3\pi}{2}$	-12
31 (B_y)	$\frac{7\pi}{4}$	-12
32 (B_y)	0	-20
33 (B_x)	$\frac{\pi}{4}$	-20
34 (B_x)	$\frac{\pi}{2}$	-20
35 (B_x)	$\frac{3\pi}{4}$	-20
36 (B_y)	π	-20
37 (B_x)	$\frac{5\pi}{4}$	-20
38 (B_y)	$\frac{3\pi}{2}$	-20
39 (B_z)	$\frac{7\pi}{4}$	-20

REFERENCES

[1] E. Komatsu and et al. "Seven-Year Wilkinson Wicrowave Anisotropy Probe Observations: Cosmological Interpretation." In: *The Astrophysical Journal Supplement Series* 192.2 (2011), p. 18.

[2] P. A. R. Ade et al. "Planck 2015 results". In: *Astronomy & Astrophysics* 594 (2016), A13.

[3] E. W. Kolb and M. S. Turner. *The Early Universe*. Addison-Wesley Publishing Company, 1993.

[4] James M. Cline. *Baryogenesis*. 2006. arXiv: `hep-ph/0609145 [hep-ph]`.

[5] L. Canetti, M. Drewes, and M. Shaposhnikov. "Matter and Antimatter in the Universe". In: *New Journal of Physics* 14.12 (2012), p. 125003.

[6] R. H. Cyburt. "Primordial nucleosynthesis for the new cosmology: Determining uncertainties and examining concordance". In: *Phys. Rev. D* 70 (2 2004), p. 023505.

[7] Particle Data Group. *Big-Bang Nucleosynthesis*. URL: `http://pdg.lbl.gov/2006/reviews/bigbangnucrpp.pdf`.

[8] P. Schmidt-Wellenburg. *The quest to find an electric dipole moment of the neutron*. 2016. arXiv: `1607.06609 [hep-ex]`.

[9] K. A. Olive, G. Steigman, and T. P. Walker. "Primordial nucleosynthesis: theory and observations". In: *Physics Reports* 333-334 (2000), pp. 389–407.

[10] M. S. Sozzi. *Discrete Symmetries and CP Violation*. Oxford University Press, 2008.

[11] T. Lancaster S. J. Blundell. *Quantum Field Theory for the Gifted Amateur*. Oxford, 2014.

[12] T. D. Lee and C. N. Yang. "Question of Parity Conservation in Weak Interactions". In: *Phys. Rev.* 104 (1 Oct. 1956), pp. 254–258.

[13] C. S. Wu et al. "Experimental Test of Parity Conservation in Beta Decay". In: *Phys. Rev.* 105 (4 Feb. 1957), pp. 1413–1415.

[14] J. W. Cronin. *CP Symmetry Violation – The Search for it's Origin*. 1980.

[15] R.F. Cowan. *Observation of Time-reversal Violation at BABAR*. 2013. arXiv: `1301.1372 [hep-ex]`.

[16] A. D. Sakharov. "Violation of CP Invariance, C asymmetry, and baryon asymmetry of the universe". In: *Pisma Zh.Eksp.Teor.Fiz.* 5 (1967), pp. 32–35.

[17] S. Dimopoulos and L. Susskind. “Baryon number of the universe”. In: *Phys. Rev. D* 18 (12 1978), pp. 4500–4509.

[18] M.E. Peskin and D.V. Shroeder. *An Introduction to Quantum Field Theory.* Westview, 1997.

[19] M. Kobayashi and T. Maskawa. “CP-Violation in the Renormalizable Theory of Weak Interaction”. In: *Progress of Theoretical Physics* 49 (1973), pp. 652–657.

[20] J. Donoghue, E. Golowich, and B. Holstein. *Dynamics of the Standard Model.* Cambridge University Press, 2014.

[21] G.C. Branco, L. Lavoura, and J.P. Silva. *CP Violation.* Clarendon Press, 1999.

[22] M. Pospelov and A. Ritz. “Electric dipole moments as probes of new physics”. In: *Annals of Physics* 318.1 (2005), pp. 119–169.

[23] D. He. “Investigation of Spin-Independent CP Violation in Neutron and Nuclear Radiative Beta Decays”. PhD thesis. University of Kentucky, 2013.

[24] T. E. Chupp et al. “Electric dipole moments of atoms, molecules, nuclei, and particles”. In: *Rev. Mod. Phys.* 91 (1 Jan. 2019), p. 015001.

[25] J. M. Pendlebury et al. “Revised experimental upper limit on the electric dipole moment of the neutron”. In: *Phys. Rev. D* 92 (9 2015), p. 092003.

[26] S. Dar. *The Neutron EDM in the SM : A Review.* 2000. arXiv: `hep-ph/0008248 [hep-ph]`.

[27] R.D. Peccei and H. Quinn. “CP Conservation in the Presence of Pseudoparticles”. In: *Physical Review Letters* 38 (June 1977), pp. 1440–1443.

[28] R. D. Peccei and H. Quinn. “Constraints imposed by CP conservation in the presence of pseudoparticles”. In: *Phys. Rev. D* 16 (6 1977), pp. 1791–1797.

[29] M. Kuster, G. Raffelt, and B. Beltran. *Axions.* Springer Berlin Heidelberg, 2007, pp. 3–17.

[30] F. Wilczek. “Problem of Strong P and T Invariance in the Presence of Instantons”. In: *Phys. Rev. Lett.* 40 (5 1978), pp. 279–282. DOI: `10.1103/PhysRevLett.40.279`. URL: `https://link.aps.org/doi/10.1103/PhysRevLett.40.279`.

[31] H.C. Cheng and D.E. Kaplan. *Axions and a Gauged Peccei-Quinn Symmetry.* 2001. arXiv: `hep-ph/0103346 [hep-ph]`.

[32] M. Kamionkowski and J. March-Russell. “Planck-scale physics and the Peccei-Quinn mechanism”. In: *Physics Letters B* 282 (1 1992), pp. 137–141. DOI: `https://doi.org/10.1016/0370-2693(92)90492-M`. URL: `http://www.sciencedirect.com/science/article/pii/037026939290492M`.

[33] I.B. Khriplovich and A.R. Zhitnitsky. “What is the value of the neutron electric dipole moment in the Kobayashi-Maskawa model?” In: *Physics Letters B* 109 (1982), pp. 490–492.

[34] A. Czarnecki and B. Krause. “Neutron Electric Dipole Moment in the Standard Model: Complete Three-Loop Calculation of the Valence Quark Contributions”. In: *Phys. Rev. Lett.* 78 (23 1997), pp. 4339–4342.

[35] J. R. Dadisman. “Magnetic Field Design to Reduce Systematic Effects in Neutron Electric Dipole Moment Measurements”. PhD thesis. University of Kentucky, 2018.

[36] S. K. Lamoreaux and R. Golub. “Experimental searches for the neutron electric dipole moment”. In: *Journal of Physics G: Nuclear and Particle Physics* 36.10 (2009), p. 104002.

[37] J. H. Smith, E. M. Purcell, and N. F. Ramsey. “Experimental Limit to the Electric Dipole Moment of the Neutron”. In: *Phys. Rev.* 108 (1957), pp. 120–122.

[38] W. B. Dress et al. “Search for an electric dipole moment of the neutron”. In: *Phys. Rev. D* 15 (1 1977), pp. 9–21.

[39] I.B. Khriplovich and S. K. Lamoreaux. *CP Violation Without Strangeness Electric Dipole Moments of Particles, Atoms, and Molecules*. Springer, 1997.

[40] C. A. Baker et al. “Improved Experimental Limit on the Electric Dipole Moment of the Neutron”. In: *Phys. Rev. Lett.* 97 (13 2006), p. 131801.

[41] S.K. Lamoreaux R. Golub D. Richardson. *Ultra-Cold Neutrons*. IOP, 1991.

[42] R. Golub and S.K. Lamoreaux. “Neutron electric-dipole moment, ultracold neutrons and polarized 3He”. In: *Physics Reports* 237 (1994).

[43] N. F. Ramsey. “A Molecular Beam Resonance Method with Separated Oscillating Fields”. In: *Phys. Rev.* 78 (1950), pp. 695–699.

[44] P. G. Harris. “The Neutron EDM Experiment”. In: (2007). arXiv: `0709.3100 [hep-ex]`.

[45] M. W. Ahmed et al. “A New Cryogenic Apparatus to Search for the Neutron Electric Dipole Moment”. In: (2019). arXiv: `1908.09937 [physics.ins-det]`.

[46] R. Golub and J. M. Pendlebury. “Super-thermal sources of ultra-cold neutrons”. In: *Physics Letters A* 53 (2 1975).

[47] C. A. Baker et al. “Experimental measurement of ultracold neutron production in 4He”. In: *Physics Letters A* 308 (1 2003), pp. 67–74.

[48] J. M. Pendlebury et al. “Geometric-phase-induced false electric dipole moment signals for particles in traps”. In: *Phys. Rev. A* 70 (3 Sept. 2004), p. 032102.

[49] S. K. Lamoreaux and R. Golub. “Detailed discussion of a linear electric field frequency shift induced in confined gases by a magnetic field gradient: Implications for neutron electric-dipole-moment experiments”. In: *Phys. Rev.* A71 (2005), p. 032104.

[50] A. L. Barabanov, R. Golub, and S. K. Lamoreaux. “Electric dipole moment searches: Effect of linear electric field frequency shifts induced in confined gases”. In: *Physical Review A* 74.5 (2006).

[51] C. M. Swank, A. K. Petukhov, and R. Golub. “Random walks with thermalizing collisions in bounded regions: Physical applications valid from the ballistic to diffusive regimes”. In: *Phys. Rev. A* 93 (6 2016), p. 062703.

[52] C. Abel et al. “Magnetic-field uniformity in neutron electric-dipole-moment experiments”. In: *Phys. Rev. A* 99 (4 2019), p. 042112.

[53] D. D. McGregor. “Transverse relaxation of spin-polarized ^3He gas due to a magnetic field gradient”. In: *Physical Review A* 41 (1990), p. 2631.

[54] J. D. Jackson. *Classical Electrodynamics*. Wiley, 1998.

[55] N. Nouri and B. Plaster. “Systematic optimization of exterior measurement locations for the determination of interior magnetic field vector components in inaccessible regions”. In: *Nuclear Instruments and Methods* A 767 (2014), pp. 92–98.

[56] N. Nouri et al. “A prototype vector magnetic field monitoring system for a neutron electric dipole moment experiment”. In: *Journal of Instrumentation* 10 (2015), P12003.

[57] N. Nouri and B. Plaster. “Sensitivity requirements for accessing interior magnetic field vector components in neutron electric dipole moment experiments via exterior boundary-value measurements”. In: *Journal of Instrumentation* 9 (2014), P11009.

[58] V. Cianciolo, J. C. Ramsey, and L. Fabris. “Design and Implementation of a Non-magnetic Cryogenic Multi-conductor Vacuum Feedthrough”. In: *in preparation* ().

[59] LakshoreCryotronics. *Technical Specifications*. URL: `https://www.lakeshore.com/products/categories/specification/temperature-products/cryogenic-accessories/cryogenic-wire`.

[60] J. M. Pendlebury and E.A. Hinds. “Particle electric dipole moments”. In: *Nuclear Instruments and Methods in Physics Research Section A: Accelerators, Spectrometers, Detectors and Associated Equipment* 440 (3 2000), pp. 471–478.

VITA

Personal Information

Name: Alina Aleksandrova

Place of Birth: Novosibirsk, Russia

Educational Institutions

M.S. Physics
University of Kentucky
December 2017

B.A. Physical Chemistry
Centre College
May 2012

Professional Positions

Graduate Research Assistant
University of Kentucky
Department of Physics and Astronomy
August 2016 – December 2019

Graduate Teaching Assistant
University of Kentucky
Department of Physics and Astronomy
August 2012 – May 2016

Publications

Ahmed, M. W., Alarcon, R., Aleksandrova, A. et al., *A New Cryogenic Apparatus to Search for the Neutron Electric Dipole Moment.*, JINST **14**, P11017 (2019). doi: 10.1088/1748-0221/14/11/p11017

Leung, K.K.H., Ahmed, M. W., Alarcon, R., Aleksandrova, A. et al., *"The neutron electric dipole moment experiment at the Spallation Neutron Source"*, arXiv:1903.02700.